Shifts in global atmospheric oxidant chemistry from land cover change

Ryan Vella[1,2], Sergey Gromov[1], Clara M. Nussbaumer[3], Laura Stecher[4,a], Matthias Kohl[1], Samuel Ruhl[1], Holger Tost[2], Jos Lelieveld[1,5], and Andrea Pozzer[1,5]

[1]Atmospheric Chemistry Department, Max Planck Institute for Chemistry, Mainz, Germany
[2]Institute for Atmospheric Physics, Johannes Gutenberg University Mainz, Mainz, Germany
[3]Institute for Atmospheric and Climate Science, ETH Zürich, Zurich, Switzerland
[4]Deutsches Zentrum für Luft- und Raumfahrt, Institut für Physik der Atmosphäre, Oberpfaffenhofen, Germany
[5]Climate and Atmosphere Research Center, The Cyprus Institute, Nicosia, Cyprus
[a]now at: Centre for Atmospheric Science, Yusuf Hamied Department of Chemistry, University of Cambridge, Cambridge, UK

Correspondence: Ryan Vella (ryan.vella@mpic.de)

Abstract.

Human activities have profoundly altered natural vegetation, primarily by converting pristine land for agriculture and grazing. Land cover change (LCC) influences the Earth system through modifications of surface albedo, roughness length, evapotranspiration, and atmospheric composition. This work investigates how LCC-driven changes in BVOC fluxes, anthropogenic surface emissions, natural soil NO emissions, and O_3 deposition fluxes affect atmospheric chemistry. The chemistry–climate model EMAC was used to compare: (1) present-day land cover, which includes areas deforested for crops and grazing, with the potential natural vegetation (PNV) cover simulated by the model, and (2) an extreme reforestation scenario where grazing land is restored to natural vegetation. Our results show that the expansion of agricultural land reduces global BVOC emissions, leading to lower annual average surface OH concentrations (-5.7%) and CO mixing ratios (-6.2%), despite increased CO from agricultural burning. Meanwhile, NO_x mixing ratios increase ($+7.8\%$) due to enhanced anthropogenic and natural soil sources. While regional ozone responses vary, global ozone production sensitivity shifts from a NO_x- to a VOC-sensitive regime. These changes influence radiative forcing: reductions in tropospheric O_3 and CH_4 lifetimes exert a combined net cooling of -60 mW m^{-2}, partially offset by warming from reduced BVOC-driven SOA formation. Reforestation of grazing areas reverses these trends to some extent, though with a weaker response.

1 Introduction

Human activities have led to substantial transformations in Earth's natural vegetation, with forests particularly impacted due to extensive conversion to agricultural land. This large-scale land cover change (LCC) has significantly influenced the Earth system, affecting nearly half of the global land surface (Hurtt et al., 2011). As a central component of Earth's biophysical and biogeochemical systems, the biosphere is markedly altered by LCC, changing major biogeochemical cycles and modifying

20 interactions with the atmosphere (Bonan, 2008). Forests, which store approximately 45% of the world's terrestrial carbon, act as a critical carbon sink, capturing and sequestering carbon that would otherwise remain in the atmosphere and contribute to global warming (Field, 2004; Pan et al., 2011). Additionally, forests play a key role in regulating the hydrological cycle through evapotranspiration, which influences atmospheric moisture levels, cloud formation, and precipitation patterns, ultimately impacting regional and global climate, including surface temperature (Betts et al., 2004; Vicente-Serrano et al., 2015; Swann

25 et al., 2012). Land cover further modulates the planetary albedo; dense forest canopies can absorb up to 90% of incoming solar radiation, thereby impacting surface reflectivity and playing a main role in the Earth's surface energy balance (Forster et al.; Gibbard et al., 2005).

The terrestrial biosphere is the primary source of biogenic volatile organic compounds (BVOCs), such as isoprene and various terpenes, which comprise nearly 90% of total volatile organic compound (VOC) emissions into the atmosphere (Guenther

30 et al., 1995). BVOCs are highly reactive, readily interacting with tropospheric oxidants to produce lower-volatility oxidation products that can partition into the aerosol phase, contributing to the formation of biogenic secondary organic aerosols (bSOA) (Heald et al., 2008) and also participating in new particle formation in pristine regions (Curtius et al., 2024).

The reactivity of BVOCs has been shown to influence global atmospheric aerosol loading, with implications for cloud properties and radiative balance (Spracklen et al., 2011; Scott et al., 2014). Numerous modeling studies have investigated how

35 land cover change (LCC) influences aerosol loading, highlighting significant atmospheric and climate impacts. In particular, deforestation has been shown to reduce the global atmospheric aerosol burden, resulting in a net radiative warming effect (Vella et al., 2025; Scott et al., 2018; Heald et al., 2008).

BVOC oxidation not only contributes to atmospheric aerosol formation but also plays a crucial role in determining the concentrations of key atmospheric oxidants, such as hydroxyl (OH) radicals, ozone (O_3), and nitrate (NO_3) radicals, thereby

40 modulating the atmosphere's oxidative capacity (Atkinson, 2000; Atkinson and Arey, 2003). The predominant reaction pathway for BVOCs is with OH radicals, which are primarily formed through the photodissociation of ozone in the presence of water vapour (Levy, 1971). While BVOCs initially deplete OH radicals through oxidation, they also contribute to OH recycling through subsequent reactions and, therefore, maintain the oxidation capacity of the atmosphere (Lelieveld et al., 2008). This complex interaction, often termed OH reformation, is essential for sustaining the troposphere's self-cleaning ability in view

45 of the high levels of reactive BVOCs emitted by vegetation. The recycling process involves the formation of peroxy radicals (RO_2), which react with nitrogen oxides (NO_x) to produce ozone (O_3) and other oxidized products. As a result, BVOCs modulate O_3 concentrations in the troposphere, which acts as both a pollutant and a greenhouse gas (Atkinson, 2000; Lelieveld et al., 2016). In addition to daytime oxidation by OH, BVOCs can also be oxidized by O_3, and NO_3 radicals during the

night, further influencing their atmospheric lifetimes and the concentrations of other trace gases (Atkinson and Arey, 2003).
50 Changes in BVOC emissions and, therefore, OH reactivity also influence the atmospheric lifetimes of methane (CH_4) and carbon monoxide (CO), as OH radicals are a primary sink of these gases (Lelieveld et al., 2016).

As forests are converted to agricultural or urban land, BVOC emissions decrease, changing the delicate balance of atmospheric chemical reactions and influencing global oxidant chemistry. Studies by Keller et al. (1991); Unger (2014) suggest that lower BVOC emissions from deforestation lead to higher OH concentrations, thereby shortening the lifetimes of CH_4 and
55 O_3 and influencing global radiative forcing. In contrast, increased BVOC emissions in future reforestation scenarios are found to have the opposite effect (Weber et al., 2024). At the same time, some studies suggest that the global atmospheric oxidizing capacity, and thus methane lifetime, remains largely unaffected by LCC (Heald and Spracklen, 2015; Ganzeveld et al., 2010; Ashworth et al., 2012). In addition to changes in BVOC emissions, land use practices involve direct emissions in the atmosphere, for example, black carbon (BC) and carbon monoxide (CO) from agricultural waste burning and NO_x and NH_3
60 emissions from manure management (Denier van der Gon et al., 2023). LCC-driven NO_x emissions account for approximately 5% of global emissions and play a key role in the HOx cycle, significantly contributing to OH budgets alongside BVOCs (Denier van der Gon et al., 2023; Elshorbany et al., 2010).

In this work, we apply the chemistry-climate model EMAC coupled with the dynamic global vegetation model (DGVM) LPJ-GUESS to investigate the impacts on oxidant chemistry from changes in BVOC emissions and surface emissions following crop
65 and grazing land expansion on potential natural vegetation (PNV). PNV refers to the type of vegetation that would naturally occur in a specific area under certain climate, soil, and environmental conditions without human influence. Land cover change is simulated through a deforestation routine in LPJ-GUESS (which simulates PNV), systematically clearing crop and grazing land areas based on 2015 land cover data. Additionally, we explore an extreme reforestation scenario where present-day grazing land is restored to natural vegetation. This work provides new insights into LCC-driven impacts on biogeochemical cycles by
70 using state-of-the-art chemical representations in EMAC coupled with interactive vegetation calculations. This work provides comprehensive estimates of changes in atmospheric composition and non-aerosol radiative effects resulting from land cover change. For the first time, we present evidence that land cover change can affect the formation sensitivity of ozone, with important implications for both air quality and climate.

2 Model description and methods

2.1 The EMAC modelling system

The EMAC (ECHAM/MESSy Atmospheric Chemistry) model is a numerical chemistry and climate modelling system, incorporating submodels that simulate tropospheric and middle atmospheric processes and their interactions with oceans, land surfaces, and human activities. It combines the ECHAM atmospheric general circulation model (GCM) (Roeckner et al., 2006) with the Modular Earth Submodel System (MESSy) framework (Jöckel et al., 2005), which structures physical-chemical pro-
80 cesses and much of the model infrastructure into modular submodels. This design enables the further development of existing processes and the addition of new submodels to introduce new or alternative process representations.

Heterogeneous and gas-phase chemistry are computed in the MECCA submodel (Sander et al., 2019), which employs the Mainz Isoprene Mechanism (MIM1) as the degradation chemical scheme (Pöschl et al., 2000; Jöckel et al., 2006). MIM1 includes over 100 gas-phase species and more than 250 reactions. While the original MIM1 mechanism accounted for isoprene oxidation by OH and O_3, here we use the an extended version, which additionally includes the oxidation of monoterpenes (treated as lumped species) by OH, O_3, NO_3, and $O(^1D)$ (Tsimpidi et al., 2014). To investigate the production and loss pathways of tropospheric chemical reactions in this study, we used the kinetic chemistry tagging method of Gromov et al. (2010). This technique quantifies the turnover rates of key tracers (in this study; OH, HO_2, NO, NO_2, O_3, CH_4, and tropospheric O_3) within the MIM1 chemistry scheme in EMAC. It provides a comprehensive assessment of OH sources and sinks, enabling the evaluation of changes in the atmosphere's oxidation capacity. By decoupling diagnostic calculations from the primary chemistry scheme, the method achieves this level of detail with minimal additional computational overhead.

Dry deposition, sedimentation, and wet deposition are simulated by the submodels DDEP, SEDI (both Kerkweg et al., 2006), and SCAV (Tost et al., 2006a), respectively. Aerosols are treated using the submodel GMXe (Pringle et al., 2010), in which aerosol are represented by seven interactive lognormal modes that span the typical size range of aerosol species. These modes are further categorised into four hydrophilic (nucleation, Aitken, accumulation, and coarse) and three hydrophobic (Aitken, accumulation, and coarse) aerosol modes. The representation of all aerosols assumes spherical particles. The properties of aerosols in each mode are fully determined by the total mass (internal mixture of contributing species), density, number concentration, median radius, and width of the lognormal distribution. After each simulation step, aerosols may transfer between modes due to size changes and shift from hydrophobic to hydrophilic modes depending on their composition. Organic aerosol species are additionally described by the Organic Aerosol Composition and Evolution (ORACLE) submodel (Tsimpidi et al., 2014, 2018), taking into account the partitioning between aerosols and the gas phase organics based on the volatility basis set (VBS) framework (Donahue et al., 2006).

Convective cloud processes are taken into account based on the approach proposed by Tost et al. (2006b), using the convection schemes from Tiedtke (1989) and Nordeng (1994). Convective cloud microphysics is solely based on temperature and moisture profiles, without accounting for the influence of aerosols on liquid droplet or ice formation processes. Large-scale stratiform clouds are described by the CLOUD submodel, which in the applied configuration, employs the original ECHAM5 cloud scheme without aerosol-cloud interactions.

LPJ-GUESS (Smith et al., 2001, 2014) is a dynamic global vegetation model (DGVM) that features an individual-based approach to modelling vegetation dynamics. These dynamics are simulated as the emergent outcome of plant growth and competition for light, space, and soil resources among woody plant individuals and a herbaceous understorey in each of a number (50 in this study) of replicate patches representing random samples of each simulated locality or grid cell. The simulated vegetation is classified into 12 plant functional types (PFTs) discriminated by growth form, phenology, photosynthetic pathway (C3 or C4), bioclimatic limits for establishment and survival and, for woody PFTs, allometry and life history strategy. The LPJ-GUESS version used in this study (v4.0) currently provides information on potential natural vegetation (PNV), and it does not incorporate LCC. In this work, however, a custom deforestation routine was integrated to constrain the PNV using deforestation maps. The deforestation maps are imported from external files and contain values ranging from 0 to 1. A value of 1 indicates

complete deforestation within the respective grid cell, while intermediate values (e.g., 0.5) represent partial deforestation. For instance, a value of 0.5 corresponds to the removal of 50% of the tree PFTs in that grid cell. The routine eliminates the tree PFTs after every simulated year and inhibits trees from establishing in the specified areas. This implementation allows us to

120   constrain the vegetation cover and address the research questions presented in this work. However, the latest version of LPJ-GUESS (v4.1) features a more advanced land cover scheme, which will be incorporated into our current LPJ-GUESS version in future developments.

2.2   EMAC–LPJ-GUESS configuration

In this work, we use the standard EMAC–LPJ-GUESS (Forrest et al., 2020; Vella et al., 2023a) coupled configuration, where

125   the vegetation in LPJ-GUESS is entirely determined by the EMAC atmospheric state, soil type, N deposition, and CO_2 fluxes, but there is no feedback from the vegetation to climate variables, except for terrestrial BVOC emissions. The roughness length and albedo are kept at constant background values. Albedo is derived from satellite climatologies, while the roughness length is based on subgrid-scale orography and satellite-derived vegetation climatology. Vegetation changes do not feed back to the hydrological cycle. We use the native bucket model in ECHAM5, which employs fixed climatological vegetation (Hagemann,

130   2002). In this setup, BVOCs are interactive tracers that can be oxidized to form secondary organic aerosols. This means that BVOCs can influence both the oxidant chemistry of the atmosphere and the aerosol load; however, this study focuses on the gaseous constituents and their respective changes.

After each simulation day, EMAC computes the average daily values of 2-meter temperature, net downwards shortwave radiation, and total precipitation and passes these state variables to LPJ-GUESS. Vegetation information (leaf area index,

135   foliar density, leaf area density distribution, and PFT fractional coverage) from LPJ-GUESS is then fed back to EMAC for the calculation of BVOC emissions. In this study, the BVOC fluxes in EMAC are calculated using the Model of Emissions of Gases and Aerosols from Nature (MEGAN) version 2.04 (Guenther et al., 2006).

MEGAN is based on the work of Guenther et al. (1993, 1995), where the BVOC emission flux is calculated as a function of PFT-specific emission factors and non-dimensional activity factors. These activity factors consider sensitivities to the canopy

140   environment, including parameters such as leaf area index (LAI), temperature, light, and leaf age. Notably, the current setup does not incorporate sensitivity to soil moisture. The parameterised canopy environment emission activity (PCEEA) algorithm is used, rather than the alternative detailed canopy environment model that calculates light and temperature at each canopy depth. The PCEEA algorithm calculates the light sensitivity within the canopy as a function of the daily average above-canopy photosynthetic photon flux density (PPFD), the solar angle and a non-dimensional factor describing the PPFD transmission

145   through the canopy.

This setup employs BVOC-aerosol-vegetation feedbacks, making vegetation and BVOC emissions sensitive to changes in temperature and above-canopy radiation (excluding diffused radiation) resulting from aerosol interactions, nevertheless, these feedbacks are partially dampened by nudging meteorological fields toward observations. BVOC emissions from this model setup were evaluated and applied in other studies (e.g. Vella et al., 2023a, b, 2025).

2.3 Experimental design

The land cover scenarios were derived from the History database of the Global Environment (HYDE v3.2) (Hurtt et al., 2011). HYDE provides a wide range of land use products, encompassing both historical and projected data. To ensure an accurate representation, we rely on HYDE's "cropland" and "grazing land" products for 2015, derived from high-resolution satellite data. These products were transformed into deforestation fraction maps (Fig. 1) to constrain the vegetation in the model. Three experiments were conducted to assess the impact of human-induced LCC on the natural land biosphere and atmospheric composition. The initial model run used simulated PNV without any deforestation. Additionally, two more model runs were conducted, incorporating deforestation. The second scenario aims to represent present-day land cover employed by deforestation based on cropland and grazing land. This scenario is referred to as "Deforested Crop and Grazing Land" (DCGL) - Fig. 1a. DCGL will also be referred to as "present-day deforestation" or "present-day land cover". The third scenario involves deforestation exclusively on cropland and is referred to as "Deforested Crop Land" (DCL) (Fig. 1b). We use the DCL scenario to evaluate the potential impact of restoring all grazing land back to its natural state, essentially creating an extreme afforestation scenario, while maintaining the present-day croplands for agricultural food production.
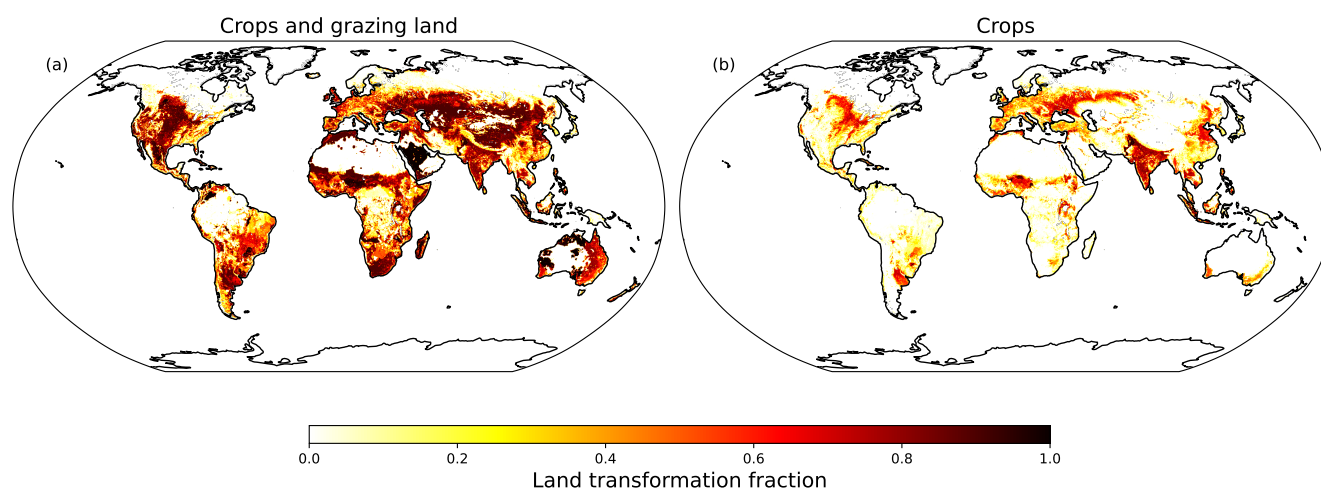
Figure 1. Deforestation maps used for the elimination of tree PFT's in LPJ-GUESS. The maps are derived from HYDE v3.2 based on the year 2015.

All simulations were conducted over 12 years (2000-2011), with the initial 2 years excluded from the analysis to ensure proper spinup and equilibrium state in the analysed data. The vegetation initial states for all simulations were taken from a previous non-chemistry 50-year run under similar atmospheric states. For this study, the simulations were performed in T63L31 resolution, i.e., approximately $1.87° \times 1.87°$ (or approx. 200×200 km at the Equator) with 31 vertical levels. The meteorological fields were nudged in the troposphere towards ERA5 data for the respective years 2000-2011. Sea surface temperature (SST) and sea ice coverage (SIC) are also inferred from the ERA5 nudging data spanning 2000 to 2012. Nudging

meteorology is important to prevent deviations in our simulations caused by feedbacks related to temperature and dynamics.

170 By implementing nudging, these feedbacks are effectively suppressed, enabling us to evaluate changes in atmospheric states solely due to perturbed emissions resulting from land cover change.

Non-GHGs tracers were initialised using climatological data from previous simulations spanning 2000 to 2020. Greenhouse gas mixing ratios, including CO_2, N_2O, CH_4, CO_2, Halons, and H_2, were prescribed at the surface level using data from the Chemistry-Climate Model Initiative (CCMI) for the year 2015 (Eyring et al., 2013). In the prognostic radiation call, these

175 radiatively active tracers were prescribed as constants based on 2015 levels, effectively decoupling changes in atmospheric chemistry (e.g., ozone) from meteorology. Furthermore, CO_2 was fixed in the vegetation scheme, ensuring that variations in CO_2 mixing ratios did not affect plant productivity. Biomass burning emissions were simulated by the BIOBURN submodel, which imports dry matter data (based on 2015) from GFEDv4.1s (Randerson et al., 2015) and employs emission factors from Andreae (2019). Anthropogenic emissions of black carbon (BC), carbon monoxide (CO), nitrogen oxides (NO_x), organic car-

180 bon (OC), sulfur dioxide (SO_2), alcohols, and organic gases were based on 2015 and sourced from the Copernicus Atmosphere Monitoring Service (CAMS-GLOB-ANTv6.2 and CAMS-GLOB-AIRv1.1) (Granier et al., 2019).

CAMS-GLOB-ANTv6.2 includes emissions from 14 sectors; power generation, refineries and fuel industries, industrial processes, road transportation, non-road transportation, ships, residential, commercial, fugitives emissions from fuels, solvents application and production, agriculture livestock, agriculture soils, solid waste and wastewater handling, and agriculture waste

185 burning (Denier van der Gon et al., 2023). The PNV run excludes surface emissions from agricultural livestock, agricultural soils, and agricultural waste burning. The DCL run excludes emissions from agricultural soils and agricultural waste burning, while the DCGL run includes all emissions, representing present-day conditions. Agricultural livestock emissions include NH_3, NMVOCs, and NO_x from manure management, as well as CH_4 from enteric fermentation. Agricultural soil emissions involve NH_3 and NO_x from agriculture-forestry-fishing activities, rice cultivation, soil emissions, and other sources. Agricultural waste

190 burning emits BC, CO, NH_3, NMVOCs, NO_x, OC, and SO_2 (Denier van der Gon et al., 2023). Anthropogenic emissions are based on 2015 data for all simulated years, with only the activated sectors varying between the runs. Table 1 summarises the experiments, including the anthropogenic emission sectors sourced from CAMS. Dry deposition calculations also incorporate interactive LAI from LPJ-GUESS, allowing us to evaluate changes in dry deposition fluxes resulting from land cover change.

Degassing volcanic climatology data were obtained from the AEROCOM project (Dentener et al., 2006). Oceanic emissions

195 and deposition were calculated online using the AIRSEA submodel (Pozzer et al., 2006; Lana et al., 2011; Fischer et al., 2012) for dimethyl sulfide (DMS), acetone (CH_3COCH_3), methanol (CH_3OH) (with an under-saturation of 6%), and isoprene (C_5H_8). Natural NO soil emissions are calculated in the ONEMIS submodel (Kerkweg et al., 2006; Ganzeveld and Lelieveld, 2004). The agricultural coverage maps used in ONEMIS were updated based on the scenario considered. Specifically, in the PNV scenario, no cultivation is assumed, while the DCGL scenario includes coverage for both crops and grazing land (Fig. 1a),

200 and the DCL scenario considers only crop coverage (Fig. 1b). Sea salt (Guelle et al., 2001) and dust emissions (Klingmüller et al., 2018) were also calculated online from ONEMIS using corresponding climate states from EMAC.

We note that all scenarios (PNV, DCGL, DCL) use the same meteorological forcing to minimise variability in BVOC emissions. This ensures that any changes in surface temperatures due to aerosol and greenhouse gas forcing are excluded. As

a result, we can investigate the impacts on atmospheric composition purely from the perspective of perturbed emissions in the present climate.

Experiment Run	Land Cover	Anthropogenic Emissions
Potential Natural Vegetation (PNV)	Natural vegetation	Excludes agriculture livestock, agricultural soils, and agricultural waste burning
Deforested Crop and Grazing Land (DCGL)	Natural vegetation without cropland and grassland	Includes all emissions (present-day conditions)
Deforested Crop Land (DCL)	Natural vegetation without cropland	Excludes agricultural soils and agricultural waste burning

Table 1. Summary of experiment runs with the corresponding land cover and anthropogenic emissions. Anthropogenic emissions are based on 2015 data for all simulated years, with only the activated sectors varying between the runs.

3 Results

3.1 Present-day land cover

3.1.1 OH reactivity

In this section, we compare tropospheric oxidant chemistry under present-day conditions with a baseline scenario featuring pristine vegetation, i.e., DCGL−PNV. The analysis accounts for changes in BVOC emissions and anthropogenic emissions associated with land cover, i.e., agricultural and livestock activities. In the PNV scenario, annual global isoprene emissions total 418.8 Tg, while monoterpene emissions reach 70 Tg. In the DCGL scenario, emissions are reduced to 307.1 Tg for isoprene and 52.5 Tg for monoterpenes, corresponding to a 25.9% decrease in total BVOC emissions. It should be noted that the BVOC emissions reported here differ from those reported in Vella et al. (2025), who used a similar model setup. In this study, BVOC emissions were scaled to better represent present-day surface O_3 mixing ratios. This adjustment was made to reproduce a mean tropospheric ozone burden of approximately 350 Tg, in line with satellite-based constraints (Gaudel et al., 2018).
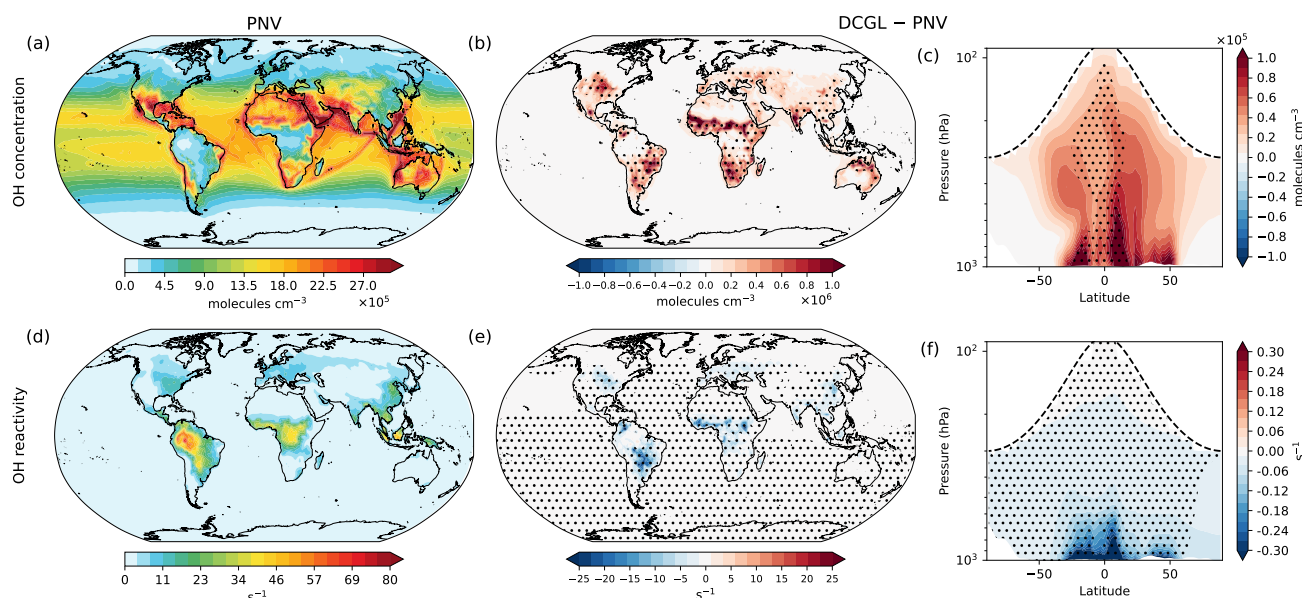
Figure 2. Changes in OH concentration and reactivity. Panels (a) and (d) display the spatial distribution of surface OH concentration and OH reactivity, respectively, under the PNV scenario. Panels (b) and (e) depict the spatial changes at the surface (DCGL − PNV), while panels (c) and (f) show the zonal average across longitudes up to 100 hPa, highlighting OH concentration and OH reactivity changes in the troposphere, respectively. The dashed line in panels (c) and (f) represents the average tropopause height. Averages include day and night OH concentration and reactivity. Dot hatching indicates a statistically significant change based on a two-tailed Student's t-test with 95% confidence.

Fig. 2 illustrates the spatial distribution of OH radicals at the surface level of the model ~~output.~~ Fig. 2a presents the OH surface concentration in the PNV scenario, with the highest concentrations observed in the tropics and mid-latitudes. This pattern

220   is primarily driven by the production of OH from the photolysis of O_3 in the presence of water vapour, along with efficient OH recycling (Lelieveld et al., 2016). Two distinct features are noticeable. First, there are patterns of low OH concentration over tropical rainforests, attributed to the high reactivity of OH with BVOCs, as shown in Fig. 2d. Second, elevated OH concentrations are present along major shipping routes. This enhancement results from the significant NO_x emissions from shipping activities, which increase the availability of ozone and other oxidants, thereby enhancing the production and regeneration of

225   OH over the oceans. The global mean surface OH concentration in the PNV scenario is 1.0×10^6 molecules cm^{-3}. Fig. 2b shows the change in surface OH concentration in the DCGL scenario relative to PNV, indicating spatial patterns that closely align with the regions of perturbed BVOC emissions due to land cover change (see Fig. S1). In the DCGL scenario, the global mean surface OH concentration increases by 5.9×10^4 molecules cm^{-3}, representing a 4.7% rise. Looking at the zonal annual mean, we see that changes in OH concentrations can extend over the entire troposphere (Fig. 2c), with changes of up to

230   1.0×10^5 molecules cm^{-3}. Most of the changes in surface OH concentration are statistically significant, while the zonal mean shows statistically significant changes across the tropical troposphere. Most of the perturbations occur in the tropics, which is expected given the dominance of tropical rainforests as the primary emitters of BVOCs. Changes in OH concentration are

statistically significant across the tropical troposphere (Fig. 2c). Fig. 2d-f illustrates the changes in OH reactivity, which represents the rate at which OH radicals react with available trace gases and is mathematically calculated as the reciprocal of the OH

235 lifetime. The reduction in BVOC emissions in the DCGL scenario leads to a global mean decrease in OH reactivity of 14.7%. As shown in the zonal mean (Fig. 2f), the largest reduction in OH reactivity is observed in the tropical lower troposphere.
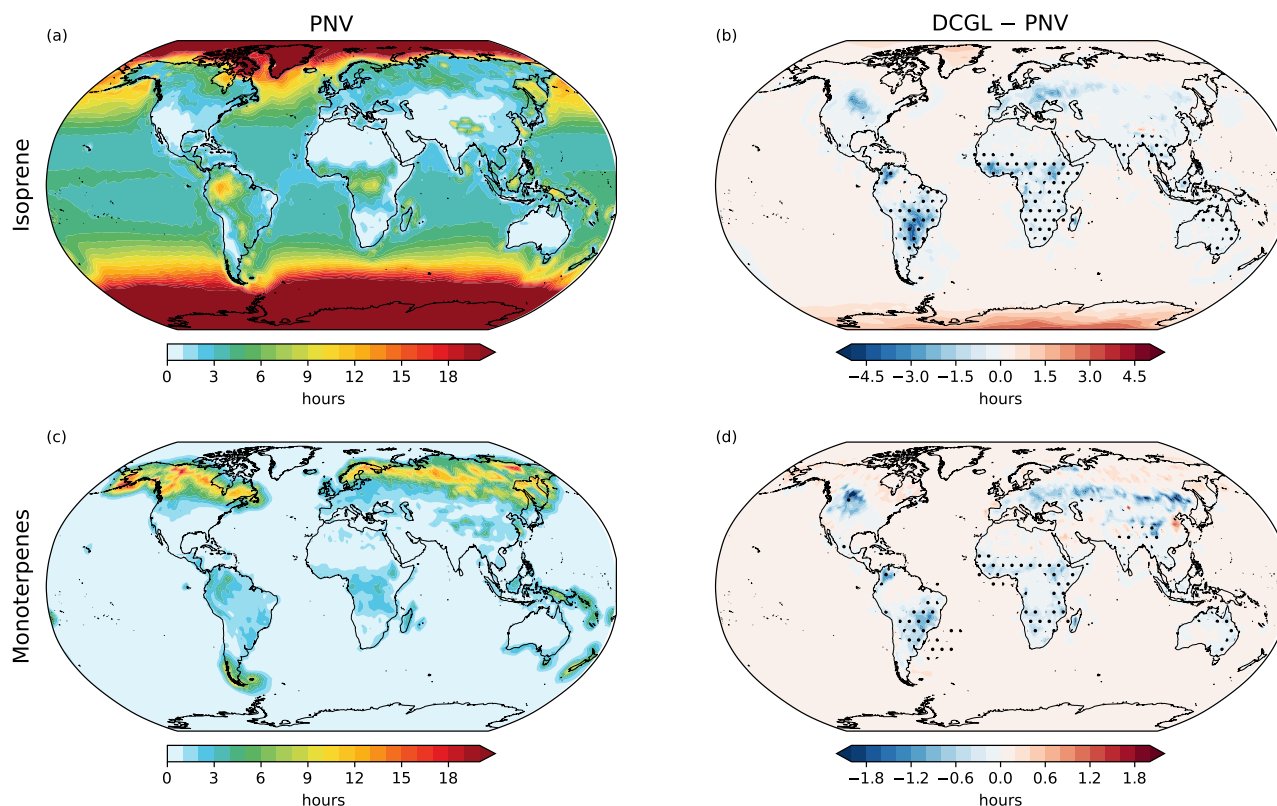
Figure 3. Spatial distribution of isoprene (a) and monoterpene (b) chemical lifetime against OH and O_3 oxidation at the surface. Panels b and d show the changes (DCGL − PNV) in isoprene and monoterpene lifetimes, respectively. Dot hatching indicates a statistically significant change based on a two-tailed Student's t-test with 95% confidence.

Fig. 3 shows the distribution of isoprene and monoterpene lifetimes at the lowest vertical level simulated by EMAC, representing the chemical lifetimes that account for the loss of BVOCs through oxidation by OH and O_3. The lifetime of BVOCs, as well as that of other species discussed later, is calculated as the ratio of the trace gas concentration to its chemical loss

240 rate, as determined using the kinetic chemistry tagging method (Gromov et al., 2010). In the PNV scenario, the annual and global mean isoprene lifetime is 10.68 hours, while in the DCGL scenario, it is 10.65 hours, reflecting a decrease of 1.6 minutes (−0.3%). Monoterpene lifetimes decreased from 61.57 minutes to 60.14 minutes, showing a reduction of 1.4 minutes (−2.3%).

Although the global relative changes are small, in regions directly affected by LCC, changes are larger with statistically significant decreases present, both in surface isoprene lifetime (by around 4 hours) and monoterpene lifetime (by over 1 hour).

245 ~~These changes are statistically significant~~. Here, we also note that the model calculations do not account for chemical loss due to NO$_3$ and O^{1}D, which may influence the actual chemical lifetime, especially for monoterpenes. However, oxidation by OH and O$_3$ remain the dominant pathways for BVOC loss.

3.1.2 Changes in key trace gases

Since OH is a major chemical sink of many atmospheric trace gases, here we address how the changes in BVOC (and therefore

250 OH) and LCC-related emissions influence the distribution and chemical lifetime of CO, NO$_x$, CH$_4$, and O$_3$. Fig.4 shows CO surface distribution and zonal means for CO mixing ratios (a-c) and lifetime (d-f). The simulations indicate that in the DCGL scenario, the global mean surface CO mixing ratio decreases by 7.5 ppbv (6.2%). Changes in CO are statistically significant over most of the globe. The zonal mean shows CO reductions throughout the troposphere. The surface CO lifetime decreases significantly over deforested regions, contributing to a global reduction in surface CO lifetime by 3.5 days.
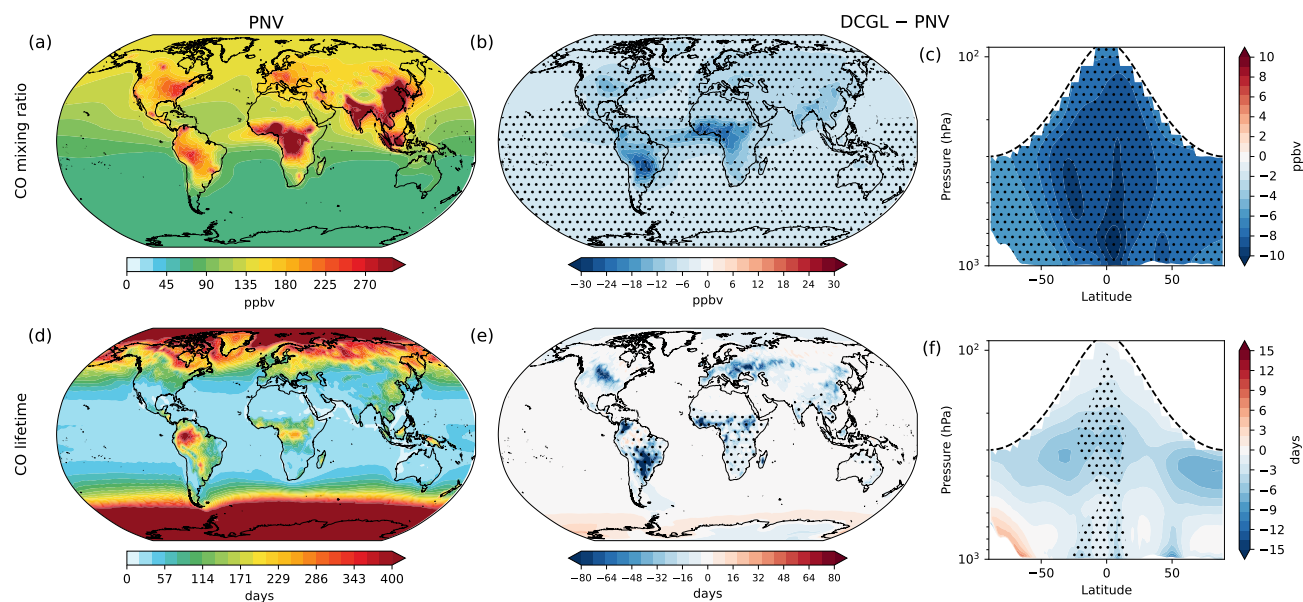
Figure 4. Changes in CO mixing ratios and lifetime. Panels (a) and (d) display the spatial distribution of surface CO mixing ratios and lifetime, respectively, under the PNV scenario. Panels (b) and (e) depict the spatial changes at the surface (DCGL − PNV), while panels (c) and (f) show the zonal average across longitudes up to 100 hPa, highlighting changes in the troposphere for CO mixing ratios and lifetime, respectively. The dashed line in panels (c) and (f) represents the average tropopause height. Dot hatching indicates a statistically significant change based on a two-tailed Student's t-test with 95% confidence.
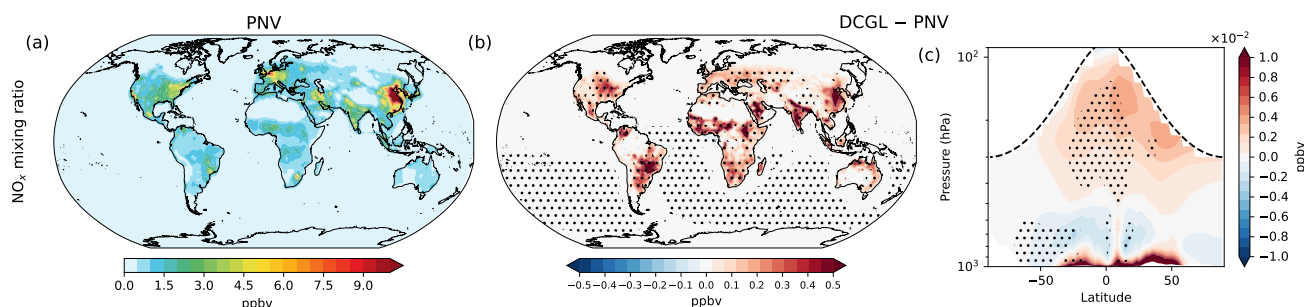
Figure 5. Same as Fig.4a-c but for NO_x.

Fig. 5 shows the distribution and changes in NO_x mixing ratios. We note that both the PNV and DGCL scenarios include anthropogenic surface emissions, which explains the elevated NO_x levels observed over the US, Europe, and particularly China (Fig. 5a). NO_x mixing ratios increase in the DGCL scenario relative to PNV, with average changes up to 1 ppbv (Fig. 5b). Globally, surface NO_x increases by 7.8%. Figure 5c shows that these changes extend into the upper tropical troposphere. In our simulations, we account for the chemical reactions influencing NO_x surface levels; however, the changes shown here also result from NO_x emission changes due to LCC and variations in natural soil NO emissions driven by the changed vegetation. We estimate a global increase of 2.84 Tg in direct NO_x emissions from agricultural and grazing activities, while soil NO emissions increase by 3.1 Tg year^{-1}. Fig. S9 shows the spatial changes in soil NO emissions.

3.1.3 Ozone production sensitivity

The global mean O_3 surface mixing ratio is 36.6 ppbv in the PNV scenario and 36.0 ppbv in the DCGL scenario, showing a slight decrease of 1.6% (Fig. 6). Fig. 6b illustrates the spatial changes in surface O_3 mixing ratios for DCGL − PNV. O_3 increases by approximately 5 ppbv over tropical South America and Central Africa and around 2 ppbv in Southeast Asia. However, background O_3 decreases, particularly over India and China. The zonal mean plot (Fig. 6c) indicates minimal variations and an overall decrease in O_3 mixing ratios across longitudes. Changes in canopy densities also lead to changes in dry deposition O_3 fluxes. In these simulations, we calculate dry deposition fluxes interactively using vegetation information from LPJ-GUESS, allowing us to infer changes in O_3 deposition. We estimate that in DGCL−PNV, O_3 deposition decreases by 2.4 Tg year^{-1} (1.5%). Spatial changes in O_3 deposition fluxes are shown in Fig. S10.
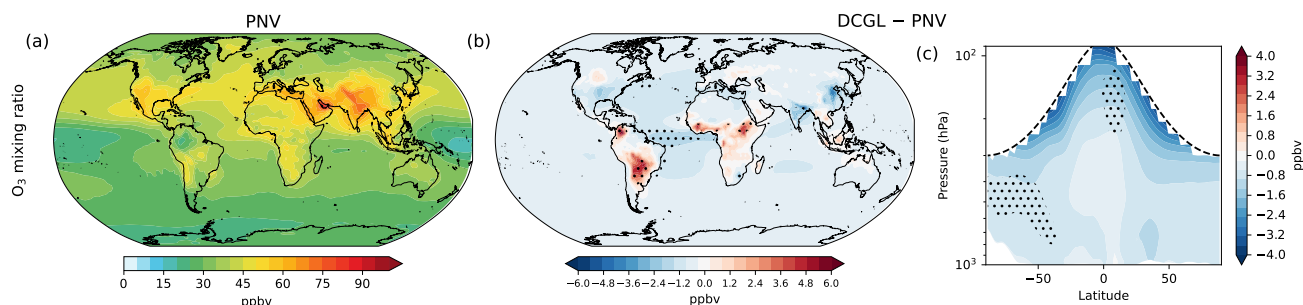
Figure 6. Same as Fig.4a-c but for O_3.

We explore changes in O_3 formation sensitivity using the metric $\alpha(CH_3O_2)$, which quantifies the proportion of methyl peroxy radicals (CH_3O_2) that react with NO, thereby promoting O_3 formation, relative to those that react with HO_2, which leads to termination of the O_3 production cycle. Ozone formation sensitivity reflects how the balance between these reaction pathways responds to changes in precursor concentrations, such as NO_x and VOCs, and is a key indicator of the chemical

275 regime governing ozone production. This relationship is described by Equation 1 (Nussbaumer et al., 2021, 2024).

$$\alpha(CH_3O_2) = \frac{k_{CH_3O_2+NO} \times [NO]}{k_{CH_3O_2+NO} \times [NO] + k_{CH_3O_2+HO_2} \times [HO_2]} \tag{1}$$

For every model grid box, $\alpha(CH_3O_2)$ was computed using surface values of NO and HO_2, with the rate constants $k(CH_3O_2 + HO_2) = 3.8 \times 10\text{-}13 \exp(780/T)$ and $k(CH_3O_2 + NO) = 2.3 \times 10\text{-}12 \exp(360/T)$ IUPAC (2025).

280 The sensitivity of O_3 production to its precursors can be characterised by investigating changes of $\alpha(CH_3O_2)$ in response to changes in NOx, as shown in Figure 7. Large increases in $\alpha(CH_3O_2)$ accompanied by small changes in NO, as seen on the steep left part of the curve, indicate NO_x-sensitive O_3 formation. In contrast, very small changes in $\alpha(CH_3O_2)$ despite increasing NO, corresponding to the nearly horizontal section on the right-hand side of the plot, indicate a VOC-sensitive regime. These two regions are connected by an intermediate section of the curve known as the transition regime. Further details on ozone

285 production sensitivity using $\alpha(CH_3O_2)$ can be found in Nussbaumer et al. (2021, 2023). The dominant O_3 production regimes can be visualized in various ways using $\alpha(CH_3O_2)$. For instance, by analyzing the gradient of the $\alpha(CH_3O_2)$ vs. NO curve, one can determine its slope and thus infer the dominant regime Nussbaumer et al. (2024). Here, we examine the y-axis of the curve by fitting a linear function to the points in the $\alpha(CH_3O_2)$ vs. NO plot. Since the y-axis ($\alpha(CH_3O_2)$ values) ranges from 0 to 1, y-intercepts close to 1 indicate an almost horizontal fit, corresponding to a VOC-sensitive regime. Conversely,

290 y-intercepts smaller than around 0.7 represent a steep curve, suggesting a NO_x-sensitive regime. Fig. 7a shows the y-intercepts for each model grid box, representing the spatial distribution of O_3 production sensitivity. The colour bar is adjusted such that values below 0.7 (NO_x-sensitive regions) appear in purple, values between 0.7 and 0.9 (transition regime) are in grey, and values between 0.9 and 1 (VOC-sensitive regions) are in green. Remote regions with low background NO fall within the NO_x-sensitive regime, whereas more polluted regions are in the VOC-sensitive regime.
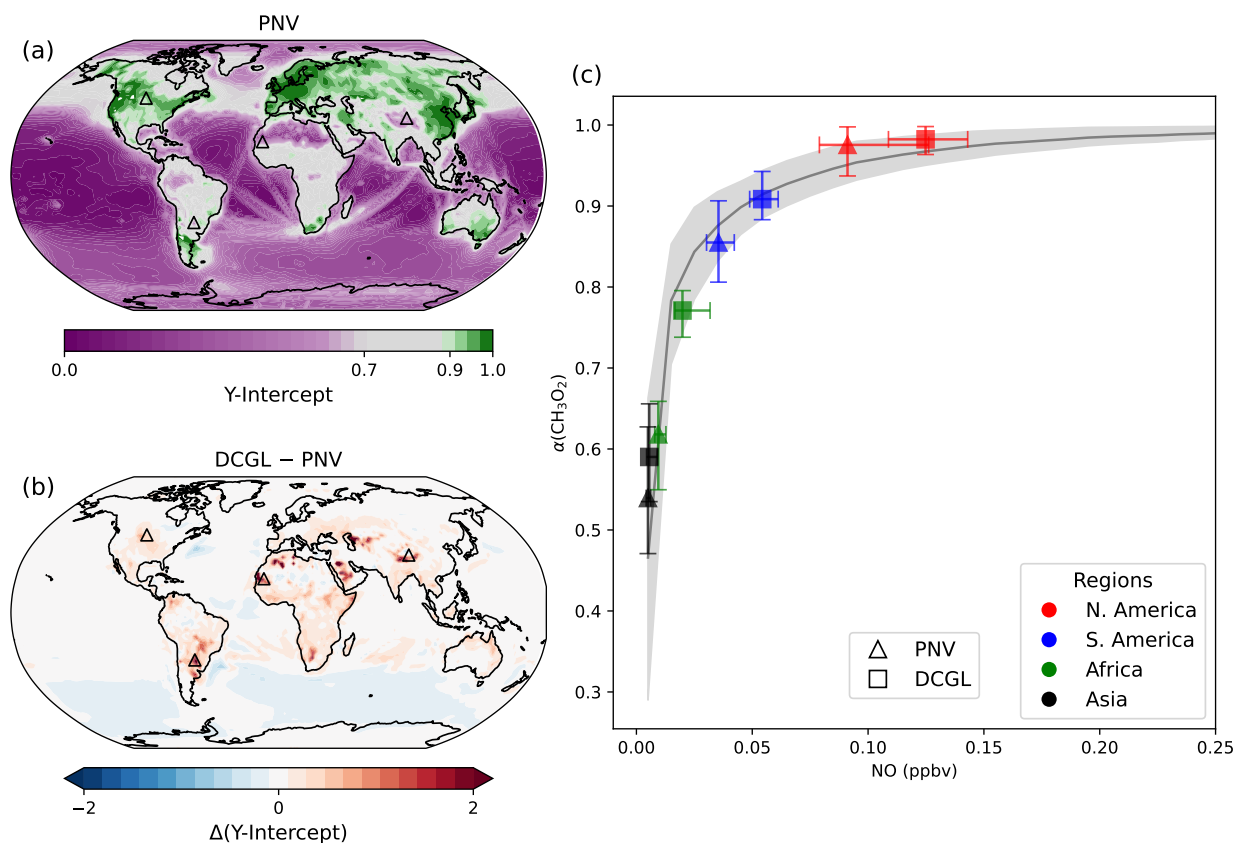
Figure 7. Changes in O_3 production sensitivity are analysed using the relationship between $\alpha(CH_3O_2)$ and NO. Panel (a) illustrates the global distribution of the y-intercept in the PNV scenario, while panel (b) displays the change in y-intercept (Δy-intercept), calculated as DCGL − PNV. Panel (c) presents the medians for $\alpha(CH_3O_2)$ vs. NO, including the background curve derived from medians of all data points, with 25th-75th percentile range shading. It also shows medians (computed over $2° \times 2°$ grid cells) for North America, South America, Africa, and Asia, with the corresponding locations marked by triangle symbols in panel (b). Triangle markers represent results from the PNV run, and square markers indicate results from the DCGL run. Both markers include error bars reflecting 25th-75th percentiles.

295   Figure 7b shows the change in the y-intercept for DCGL − PNV, indicating that in regions affected by deforestation, the $\alpha(CH_3O_2)$ vs. NO curve shifts towards larger values for $\alpha(CH_3O_2)$ and NO, suggesting a transition toward the VOC-sensitive regime. Four regions across North America, South America, Africa, and Asia were selected as examples to reproduce the changes in the average $\alpha(CH_3O_2)$ vs. NO for these regions under the PNV (triangle markers) and DCGL (square markers) scenarios (Fig. 7c). The plot includes a curve representing the background (i.e., mean of all grid points binned to NO) with 300   a 1-sigma shading. Across all selected regions, there is a clear shift towards VOC sensitivity. These shifts are, however, not

uniform across all regions. We estimate an increase in the ozone mixing ratio of 0.63 ppbv (+1.6%) in North America, 3.26 ppbv (+10.5%) in South America, 0.33 ppbv (+0.8%) in Africa, and 0.34 ppbv (+0.54%) in Asia. While regions already dominated by VOC sensitivity show relatively little change in $\alpha(CH_3O_2)$ and, consequently, in O_3 formation, more significant shifts occur in regions where the system might transition from a NO_x-sensitive to a VOC-sensitive regime. For example, in South America, we observe a substantial shift in $\alpha(CH_3O_2)$, where ozone production sensitivity is pushed towards VOC sensitivity, resulting in a strong increase in O_3 mixing ratios (+10.5%) in this region.

3.1.4 Ozone and methane radiative effects

A detailed evaluation of the radiative effects resulting from changes in the global aerosol burden due to LCC-driven changes in biogenic secondary organic aerosols formed through the oxidation of BVOCs has been presented in Vella et al. (2025). In this study, we focus specifically on the radiative effects arising from changes in O_3 and CH_4 concentrations. Fig. 8a illustrates the changes in the top-of-the-atmosphere (TOA) radiative effects resulting from variations in O_3 concentrations under the DCGL scenario relative to PNV. RE_{O_3} is computed using diagnostic radiation employing interactive O_3 tracer concentrations, thus yielding the instantaneous radiative effect. LCC under present-day conditions, compared to natural vegetation, leads to a small global cooling effect of -10 mW m^{-2}, which is a change of less than 1%.
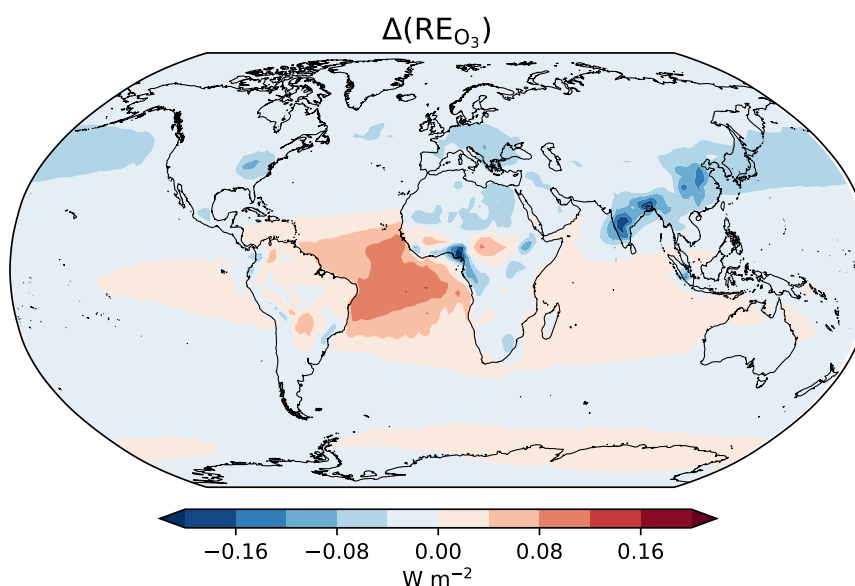
Figure 8. Radiative effects due to O_3 changes from the deforestation (DCGL $-$ PNV) scenario, showing the top-of-the-atmosphere (TOA) radiative effect (shortwave + longwave).

315   Differently than O_3, in our simulations, we prescribe surface methane concentrations, meaning that the radiative effect from methane changes cannot be directly evaluated from the model output. We therefore first compute the CH_4 equilibrium mixing ratio, which is the mixing ratio the model is expected to adjust if CH_4 was not prescribed at the lower boundary.

$$[CH_4]_{eq} = [CH_4]_{ref} \cdot \left(\frac{\tau_{exp}}{\tau} \right)^f$$

where $[CH_4]_{ref}$ is the simulated CH_4 mixing ratio (i.e., the prescribed CH_4 at the surface consistent with DCGL, as they
320   represent the "observed" present-day, which includes land use changes), and τ_{exp} and τ are the CH_4 lifetimes from the perturbed (PNV) and reference (DCGL) simulation, respectively (Fiore et al., 2009). f is a feedback factor that accounts for the influence of CH_4 changes on its lifetime, resulting in subsequent adjustments to the CH_4 mixing ratio. The value of f is estimated to range between approximately 1.2 and 1.5 (Fiore et al., 2009; Voulgarakis et al., 2013; Stevenson et al., 2013; Thornhill et al., 2021; Stevenson et al., 2020). We find that the global mean CH_4 lifetime (against OH, $O(^1D)$, and Cl) is 10.6 years in the
325   PNV simulation, compared to 10.1 years in DGCL, representing a decrease of 165 days (4.3%). This reduction is primarily due to enhanced OH concentrations in DGCL. With a reference CH_4 mixing ratio of $[CH_4]_{ref} = 1.91$ ppmv, this suggests a reduction of the global CH_4 mixing ratio to 1.78 ppmv in PNV (based on $f = 1.5$). Following the approach used by Etminan et al. (2016), this corresponds to a stratospheric-adjusted radiative effect (RE) of -50 mW m^{-2}, reflecting the expected CH_4 decrease due to deforestation.

3.2   Grazing-land restoration scenario

In this section, we examine the impacts of restoring all grazing land to natural vegetation, i.e. DCGL$-$DCL. These analyses effectively represent atmospheric chemistry changes in an extreme reforestation scenario. Figure 9 summarises the shifts in atmospheric states resulting from restoring present-day grazing land to its natural state.

The global mean surface OH concentration decreases by 4.4×10^4 molecules cm^{-3} (4.0%) (Fig. 9a), with reductions pri-
335   marily over reforested areas. This leads to longer BVOC lifetimes (Fig. 9b), with increases of up to 4 hours in regions where trees replace grazing land. The isoprene lifetime increases by 1.04 minutes, while the monoterpene lifetime increases by 1.46 minutes. Figures 9c–e show changes in surface CO, NO_x, and O_3. CO increases by 4.6 ppbv (4.0%), NO_x by 0.02 ppbv (5.0%), and O_3 increases by 0.02 ppbv (0.7%). Fig. 9f shows changes in the y-intercept of the $\alpha(CH_3O_2)$ vs. NO curve. Here, O_3 production sensitivity shifts toward the NO_x-sensitive regime. Additional plots, similar to those in the main text, but for
340   DCGL$-$DCL, are provided in the supplementary material.
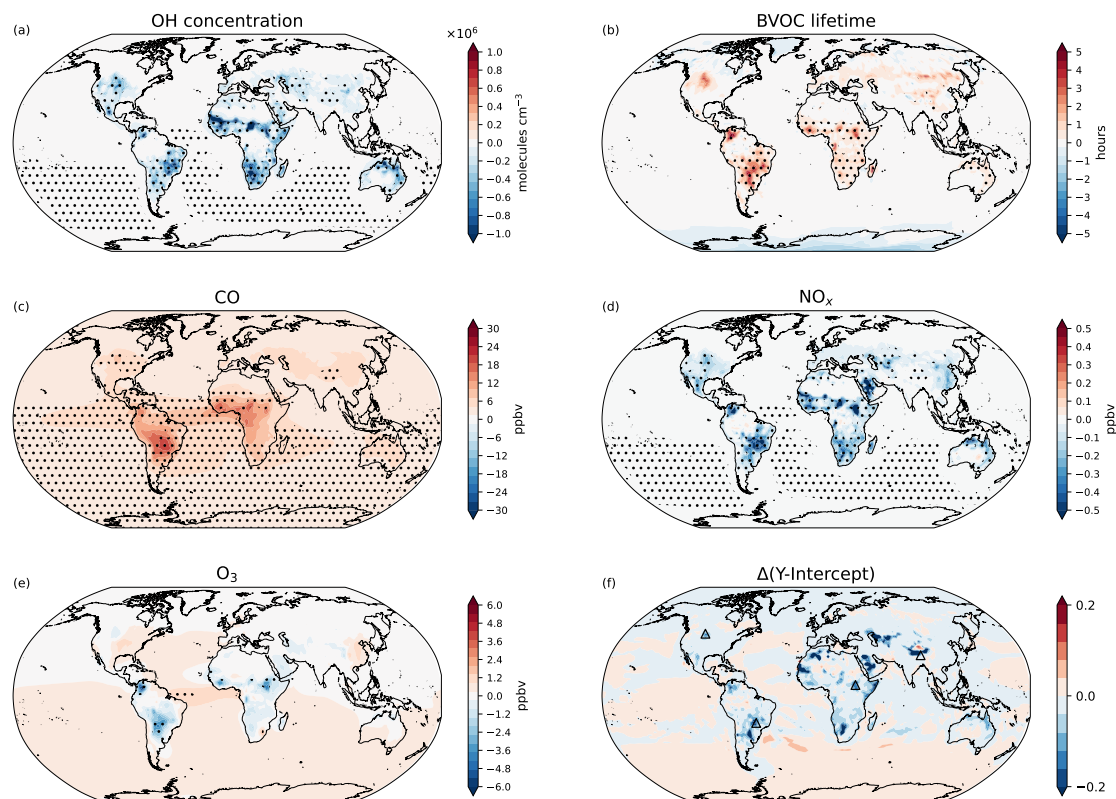
Figure 9. Absolute changes in atmospheric states resulting from the restoration of present-day grazing land (DCGL − DCL). Maps show variations in (a) surface OH concentration (b) BVOC lifetime, (c) CO surface mixing ratio, (d) NO_x surface mixing ratio, (e) O_3 surface mixing ratio, and (e) changes in O_3 production sensitivity. Dot hatching indicates a statistically significant change based on a two-tailed Student's t-test with 95% confidence.

4   Discussion

Changes in land cover can substantially impact atmospheric processes and, in turn, the climate system. Numerous studies have explored how land cover changes alter the climate by affecting carbon fluxes, the hydrological cycle, surface albedo, aerosols, and atmospheric chemistry. This study specifically examines the impact of land cover changes on atmospheric composition

345   from perturbed BVOC and anthropogenic emissions associated with LCC. In Vella et al. (2025), we showed that the model setup employed in this work can represent changes in vegetation cover and BVOC emissions in the scenarios considered (i.e., PNV, DCGL, DCL). This study, which focuses on atmospheric chemistry, introduces two key modifications relative to the setup in Vella et al. (2025): aerosol–cloud interactions not considered reduce meteorological variability and associated changes in transport, and MEGAN-derived BVOC fluxes are tuned to better represent the present-day O_3 burden.

350   Additionally, dry deposition fluxes are computed interactively using LAI information from LPJ-GUESS, and soil NO emissions were also modified to account for changes in land cover. We emphasise that while vegetation states are fully determined by EMAC prognostic variables, only BVOC emissions and dry deposition fluxes are interactively fed back from the vegetation calculations. This means that other feedbacks associated with land cover change (e.g., changes in evapotranspiration, albedo, roughness length, and aerosols) are suppressed, allowing us to focus solely on the impact of land cover change on oxidant

355   chemistry via perturbed BVOC fluxes and surface emissions from LCC. Table 2 summarises the changes in vegetation and atmospheric states for the different scenarios considered in this work: (i) the difference between 2015 land cover and natural vegetation (DCGL − PNV) and (ii) the impact of restoring grazing land relative to 2015 land cover (DCL − DCGL). Changes are presented in both absolute and relative terms.

	DCGL−PNV		DCL−DCGL	
	Abs.	Rel.	Abs.	Rel.
Tree cover	−1026 Mha	−18.0%	+600 Mha	+12.9%
Vegetation biomass	−64 PgC	−11.2%	+43 PgC	+8.6%
Isoprene emis	−111.7 Tg	−26.7%	+69.2 Tg	+22.5%
Monoterpenes emis	−17.5 Tg	−25.0%	+10.7 Tg	+20.5%
Isoprene lifetime	−1.64 min	−0.3%	+1.04 min	+0.2%
Monoterpenes lifetime	−1.43 min	−2.3%	+1.46 min	+2.4%
OH concentration	$+5.9 \times 10^4$ molec cm^{-3}	5.7%	-4.4×10^4 molec cm^{-3}	−4.0%
CO mixing ratio	−7.5 ppbv	−6.2%	+4.6 ppbv	+4.0%
NO$_x$ mixing ratio	+0.03 ppbv	+7.8%	−0.02 ppbv	−5.0%
Soil NO flux	+3.1 Tg year^{-1}	+51.3%	−2.3 Tg year^{-1}	−25.0%
O$_3$ mixing ratio	−0.06 ppbv	−1.6%	+0.02 ppbv	+0.7%
O$_3$ deposition flux	−2.4 Tg year^{-1}	−1.5%	+1.1 Tg year^{-1}	+0.7%
CH$_4$ lifetime	−165 days	−4.7%	+117 days	+3.2%
RE$_{O_3}$	−10 mW m^{-2}	-	+1.3 mW m^{-2}	-
RE$_{CH_4}$	−50 mW m^{-2}	-	+30 mW m^{-2}	-

Table 2. Changes in vegetation and atmospheric variables for the two land cover scenarios: present-day land cover vs. natural vegetation (DCGL−PNV) and restoration of grazing land vs. present-day land cover (DCL−DCGL). Tree cover, vegetation biomass, isoprene emissions, and monoterpenes emissions are global yearly sums, while OH concentration, CO, NO, O$_3$ mixing ratios, CH4 lifetime, RE$_{O_3}$, and RE$_{CH_4}$ are global yearly means. Concentrations and lifetime are based on the model's surface level, while the radiative effects refer to the top of the atmosphere (TOA).

The oxidation capacity of the atmosphere is primarily controlled by hydroxyl (OH) radicals in the troposphere. Consistent with previous studies, our model calculations show the highest OH concentrations in the tropical troposphere, with a global mean tropospheric OH of 11.0×10^5 molecules cm^{-3} in the DCGL scenario, representative of present day conditions. This value is close to the 11.3×10^5 molecules cm^{-3} reported by Lelieveld et al. (2016) and the multimodel mean of $(11.1 \pm 1.6) \times 10^5$ molecules cm^{-3} derived for the year 2000 by Naik et al. (2013). The small deviations are likely due to differences in model setups. Here, we use surface emissions based on the year 2015, while meteorological fields are nudged at the surface using 2000–2011 conditions. As per our investigation in this work, differences in vegetation representation, as well as uncertainties in global VOC budgets, may also contribute to changes in OH budgets.

Present-day land cover, relative to natural vegetation, increases the global mean surface OH concentration by 5.7%, while restoring current present-day grazing land would decrease it by 4.0%. In both scenarios, surface OH changes correspond to regions where BVOC emissions were perturbed due to deforestation and reforestation, respectively. EMAC suggests that land-cover-driven BVOC emissions perturb OH concentrations in the tropical troposphere, with relatively strong changes extending to the upper troposphere (Fig.2c & Fig. S2c). While these changes are statistically significant, they remain small relative to the BVOC emissions changes (-25.9% in the deforestation scenario and $+21.3\%$ in the reforestation scenario). This is due to the efficient recycling of OH radicals, which buffers the global OH burden (Lelieveld et al., 2008). Our simulations include OH recycling chemistry as detailed in Lelieveld et al. (2016). Wu et al. (2012) suggests a global annual tropospheric OH mean of 11.3×10^5 molecules cm^{-3} based on the year 2000. Simulations that account for climate change, CO$_2$ trends, and land use change project an OH increase of 1% in 2050 and a decrease of 2% in 2100. One should note these changes reported in Wu et al. (2012) are primarily driven by the projected increase in BVOC emissions (isoprene: +10% in 2050 and +25% in 2100) due to climate warming. Our findings also align with Ganzeveld et al. (2010), who suggest that significant local changes in the atmospheric oxidizing capacity are confined to areas influenced by ~~LLC,~~ mostly in the tropics. Scott et al. (2018) estimates that complete global deforestation increases the annual tropospheric mean OH concentration from 13.6×10^5 to 14.6×10^5 molecules cm^{-3} (+7.4%). This agrees with the 5.7% increase simulated by EMAC under more realistic land cover changes.

Table S1 highlights the differences in prescribed global annual emission burdens across the simulations, with DCGL−PNV showing increases of 37.1 Tg in CO, 35.25 Tg in NH$_3$, and 2.84 Tg in NO$_x$. On the other hand, DCL−DCGL shows a decrease of 37.1 Tg in CO, 26.58 Tg in NH$_3$, and 2.64 Tg in NO$_x$, reflecting the elimination of emissions from grazing land practices in this scenario, where these areas are restored.

We report a 7.5 ppbv decrease in the mean annual surface CO mixing ratio in the 2015 land cover scenario relative to pristine vegetation. As OH is the primary sink for CO, the increased availability of OH radicals enhances CO depletion. Notably, this 6.2% reduction occurs despite an additional 37.1 Tg annual CO emissions burden from grazing land (mostly biomass burning), highlighting the dominant role of atmospheric oxidation in regulating CO levels (Granier et al., 2000). In DCL−DCGL, the 37.1 Tg decrease in surface emissions from grazing land is offset by increased BVOC emissions from reforestation, which lead to a reduction in OH radicals. This reduction in OH limits CO depletion, resulting in a net increase of 4.6 ppbv (4.0%).

In the DCGL−PNV scenario, a 2.84 Tg increase in prescribed NO$_x$ emissions leads to a 7.8% rise in the global mean NO$_x$ mixing ratio. This increase is also partially driven by higher soil NO emissions (+3.1 Tg) due to deforestation, as reduced

canopy deposition enhances their release, consistent with (Ganzeveld and Lelieveld, 2004). Despite the increased availability

395 of OH, the substantial rise in NO_x emissions outweighs the enhanced removal of NO_x via oxidation by OH. Similarly, in the DCL−DCGL scenario, a 2.64 Tg reduction in NO_x emissions, along with a 2.3 Tg decrease in soil NO emissions, dominates surface NO_x levels, leading to a 6.4% decline.

LCC changes significant ~~shifts~~ in both NO_x and VOC emissions, influencing the O_3 production and distribution. Table 2 confirms that, globally, surface ozone remains relatively unchanged; however, significant regional variations are evident

400 (Fig. 6b). These changes are closely linked to ozone formation sensitivity. As shown in Fig. 6b, urban and polluted areas, which are typically VOC-limited, experience ozone production constrained by VOC availability. In these regions, reduced BVOC emissions lead to lower peroxy radical (RO_2) concentrations, slowing the conversion of NO to NO_2 and ultimately reducing O_3 formation rates. This results in the observed decrease in surface O_3 mixing ratios. Conversely, in rural areas of tropical South America, Africa and SE Asia, ozone production is more sensitive to NO_x levels. Increased surface NO_x

405 (from farming) enhances NO_2 formation, which photolyses to produce O_3, leading to higher regional O_3 levels. Our analysis using the sensitivity metric $\alpha(CH_3O_2)$ indicates that, under present-day conditions compared to pristine vegetation, ozone production shifts towards a VOC-sensitive regime, except over the Southern Ocean, which appears to shift towards a NO_x-sensitive regime (Fig. 7b). In remote marine environments, such as the Southern Ocean, BVOC concentrations are extremely low, making ozone formation primarily NO_x-sensitive. In these regions, the perturbation of BVOCs has minimal impact on

410 ozone production, and even a slight increase in background NO_x levels can significantly enhance ozone production through NO_x-dependent photochemical processes.

Hotspots where ozone production sensitivity changes drastically were identified and plotted on an $\alpha(CH_3O_2)$ vs. NO curve. The selected locations are Central North America (100°W, 46°N), Southeastern South America (59°W, 28°S), West Africa (11°W, 20°N), and South Asia (91°E, 34°N). Fig. 7c confirms that, in these regions, ozone production generally shifts toward

415 a VOC-sensitive regime. While South America and Africa largely remain in the transition regime, a clearer shift is observed in North America, where ozone production moves from the transition regime to VOC sensitivity. In DCL−DCGL, we observe opposite signals (Fig. S7), with ozone production sensitivity shifting toward a NO_x-sensitive regime. Li et al. (2015) showed that reforestation efforts in southern China increased BVOC emissions. This led to a reduction in surface O_3 by 1.6–2.5 ppbv in rural regions but caused an increase in O_3 peaks by up to 2.0–6.0 ppbv in VOC-limited urban areas. It is important to note

420 that we limit changes in surface emissions related to LCC and do not account for past or future variations in anthropogenic emissions, which would also influence ozone production sensitivity (Wang et al., 2020).

Tropospheric O_3 and CH_4 are potent greenhouse gases with global warming potentials (GWPs) significantly higher than CO_2. As a result, even small changes in the abundance of these gases can impact the climate (Forster et al., 2007). We find that deforestation has had an indirect cooling effect on the climate, with RE_{O_3} and RE_{CH_4} of -10 mW m^{-2} and -50.0 mW m^{-2},

425 respectively. In contrast, restoring grazing land would result in a warming by 1.3 mW m^{-2} for O_3 and 40.0 mW m^{-2} for CH_4. We also point out that changes in RE_{O_3} were found not to be statistically significant.

Scott et al. (2018) estimates a global annual mean tropospheric RE of CH_4 at -70 mW m^{-2} and of O_3 at 170 mW m^{-2} in a complete deforestation scenario. However, in Scott et al. (2018), RE_{CH_4} is inferred from changes in steady-state CH_4

concentration, whereas in our calculations, RE_{CH_4} is derived from changes in CH4 lifetime due to prescribed surface emis-
sions. Additionally, RE_{O_3} in Scott et al. (2018) is calculated using a radiative kernel approach that accounts for stratospheric
adjustments over the annual cycle, while we compute REO_3 based on instantaneous radiative effects in the model.

Weber et al. (2024) estimates an effective ~~radaitve~~ effect (ERE_{O_3}) between 32 and 57 mW m^{-2}, and ERE_{CH_4} between 7 and
20 mW m^{-2} in a future reforestation scenario. For a fair comparison with the ERE_{CH_4} reported in Weber et al. (2024), we have
to scale our -50 mW m^{-2} to -43 mW m^{-2} to account for additional chemical production of ozone and stratospheric water
vapour, and accounting for the negative cloud adjustment including SW absorption by CH$_4$ (Thornhill et al., 2021; Smith et al.,
2018; Etminan et al., 2016). This scaling, therefore, converts our surface-adjusted RE (-50 mW m^{-2}) to ERF (-43 mW m^{-2})
corresponding to the value reported in Weber et al. (2024). We also note that we calculate the instantaneous RE_{O_3}, excluding
climate feedbacks or time-lagged responses (such as temperature changes or water vapour feedback).

Given the complex response of O$_3$ to BVOC changes, RE_{O_3} exhibits high spatial and interannual variability compared to
CH$_4$. As shown in Fig. 8, the top-of-atmosphere (TOA) RE_{O_3} includes regional hotspots corresponding to increases in surface
ozone mixing ratios in DCGl$-$PNV over North America, Europe, and Asia (Fig. 6b). Our findings are consistent with previous
work, which shows a negative RE for O$_3$ and CH$_4$ linked to deforestation and a positive one linked to reforestation (Unger,
2014; Thornhill et al., 2021). We show ~~that changes~~ in RE_{O_3} ~~are~~ not as strong as previously suggested (Scott et al., 2018;
Weber et al., 2024). Nevertheless, this discrepancy may partly arise from the slightly different model setups and methods used
to estimate the radiative effects.

5 Conclusions

Understanding the effects of land use changes on atmospheric composition is essential for assessing the impact of human
activities on the Earth system, both historically and in the future. This study provides a detailed analysis of two land-use change
scenarios, examining how variations in BVOC emissions and emissions from crop and grazing land affect atmospheric oxidant
chemistry. We focus on tropospheric changes in OH radicals, CO, NO$_x$, O$_3$, and CH$_4$, as well as their radiative effects. We find
that present-day deforestation relative to pristine vegetation decreases global BVOC emissions. These reductions significantly
alter atmospheric chemistry, particularly through their impact on oxidant levels. Global surface OH concentrations decrease by
5.7%, leading to a reduction in the oxidation of CO and a consequent 6.2% decrease in its surface mixing ratio. In contrast,
the global surface NO$_x$ mixing ratio increases by 7.8%, primarily due to enhanced emissions from cropland and grazing land,
as well as increased soil NO emissions. Ozone changes are more complex, with a global surface mean mixing ratio decrease
of less than 1 ppbv (about 1%). However, significant regional variations occur, driven by shifts in ozone production regimes.
Our assessment using the sensitivity metric $\alpha(CH_3O_2)$ indicates a consistent shift towards a VOC-sensitive ozone formation
regime in the deforestation scenario. Shorter lifetimes of O$_3$ and CH$_4$ result in a small cooling radiative effect of 10 mW m^{-2}
and 50 mW m^{-2}, respectively. This cooling partially offsets the warming effect from reduced biogenic SOA, which Vella et al.
(2025) estimates to be 60.4 mW m^{-2}. Ongoing land cover change may continue to reduce vegetation cover in pristine forested
regions. In areas with low background concentrations of nitrogen oxides, such changes can promote further increases in surface

ozone levels due to a shift toward VOC-sensitive ozone production. Increased BVOC emissions from large-scale reforestation efforts impact atmospheric oxidant chemistry in a manner largely opposite to the deforestation scenario, albeit with a weaker magnitude.

465 *Code and data availability.* The Modular Earth Submodel System (MESSy, doi:10.5281/zenodo.8360186) is continuously further developed and applied by a consortium of institutions. The usage of MESSy and access to the source code is licenced to all affiliates of institutions which are members of the MESSy Consortium. Institutions can become a member of the MESSy Consortium by signing the MESSy Memorandum of Understanding. More information can be found on the MESSy Consortium Website (http://www.messy-interface.org).

The model outputs relevant to this study are permanently stored in the Zenodo repository and are accessible via . Analysis scripts are
470 available upon request from the corresponding author.

Author contributions. RV, AP, and HT conceptualised the study. RV prepared the model setup and conducted the simulations. SG contributed to the implementation of kinetic chemistry tagging, while CMN provided guidance on the O_3 production sensitivity analysis. LS assisted with calculations related to radiation effects. MK and SR helped with analysis scripts and supported the interpretation of some results. AP and JL supervised the project. All authors actively discussed the results and participated in reviewing and editing the manuscript.

475 *Competing interests.* At least one of the (co-)authors is a member of the editorial board of *Atmospheric Chemistry and Physics*. The peer-review process was guided by an independent editor, and the authors also have no other competing interests to declare.

Acknowledgements. The model simulations have been performed at the German Climate Computing Centre (DKRZ) through support from the Max Planck Society and the JGU Mainz. HT acknowledges funding support from the Deutsche Forschungsgemeinschaft (DFG, German Research Foundation) – TRR 301 – Project-ID 428312742.

References

Andreae, M. O.: Emission of Trace Gases and Aerosols from Biomass Burning – an Updated Assessment, Atmospheric Chemistry and Physics, 19, 8523–8546, https://doi.org/10.5194/acp-19-8523-2019, 2019.

Ashworth, K., Folberth, G., Hewitt, C. N., and Wild, O.: Impacts of Near-Future Cultivation of Biofuel Feedstocks on Atmospheric Composition and Local Air Quality, Atmospheric Chemistry and Physics, 12, 919–939, https://doi.org/10.5194/acp-12-919-2012, 2012.

Atkinson, R.: Atmospheric Chemistry of VOCs and NOx, Atmospheric Environment, 34, 2063–2101, https://doi.org/10.1016/S1352-2310(99)00460-4, 2000.

Atkinson, R. and Arey, J.: Gas-Phase Tropospheric Chemistry of Biogenic Volatile Organic Compounds: A Review, Atmospheric Environment, 37, 197–219, https://doi.org/10.1016/S1352-2310(03)00391-1, 2003.

Betts, R. A., Cox, P. M., Collins, M., Harris, P. P., Huntingford, C., and Jones, C. D.: The Role of Ecosystem-Atmosphere Interactions in Simulated Amazonian Precipitation Decrease and Forest Dieback under Global Climate Warming, Theoretical and Applied Climatology, 78, https://doi.org/10.1007/s00704-004-0050-y, 2004.

Bonan, G. B.: Forests and Climate Change: Forcings, Feedbacks, and the Climate Benefits of Forests, Science, 320, 1444–1449, https://doi.org/10.1126/science.1155121, 2008.

Curtius, J., Heinritzi, M., Beck, L. J., Pöhlker, M. L., Tripathi, N., Krumm, B. E., Holzbeck, P., Nussbaumer, C. M., Hernández Pardo, L., Klimach, T., Barmpounis, K., Andersen, S. T., Bardakov, R., Bohn, B., Cecchini, M. A., Chaboureau, J.-P., Dauhut, T., Dienhart, D., Dörich, R., Edtbauer, A., Giez, A., Hartmann, A., Holanda, B. A., Joppe, P., Kaiser, K., Keber, T., Klebach, H., Krüger, O. O., Kürten, A., Mallaun, C., Marno, D., Martinez, M., Monteiro, C., Nelson, C., Ort, L., Raj, S. S., Richter, S., Ringsdorf, A., Rocha, F., Simon, M., Sreekumar, S., Tsokankunku, A., Unfer, G. R., Valenti, I. D., Wang, N., Zahn, A., Zauner-Wieczorek, M., Albrecht, R. I., Andreae, M. O., Artaxo, P., Crowley, J. N., Fischer, H., Harder, H., Herdies, D. L., Machado, L. A. T., Pöhlker, C., Pöschl, U., Possner, A., Pozzer, A., Schneider, J., Williams, J., and Lelieveld, J.: Isoprene Nitrates Drive New Particle Formation in Amazon's Upper Troposphere, Nature, 636, 124–130, https://doi.org/10.1038/s41586-024-08192-4, 2024.

Denier van der Gon, H., Gauss, M., Granier, C., Arellano, S., Benedictow, A., Darras, S., Dellaert, S., Guevara, M., Jalkanen, J.-P., Krueger, K., Kuenen, J., Liaskoni, M., Liousse, C., Markova, J., Prieto Perez, A., Quack, B., Simpson, D., Sindelarova, K., and Soulie, A.: Documentation of CAMS Emission Inventory Products, https://doi.org/10.24380/Q2SI-TI6I, 2023.

Dentener, F., Kinne, S., Bond, T., Boucher, O., Cofala, J., Generoso, S., Ginoux, P., Gong, S., Hoelzemann, J. J., Ito, A., Marelli, L., Penner, J. E., Putaud, J.-P., Textor, C., Schulz, M., van der Werf, G. R., and Wilson, J.: Emissions of Primary Aerosol and Precursor Gases in the Years 2000 and 1750 Prescribed Data-Sets for AeroCom, Atmospheric Chemistry and Physics, 6, 4321–4344, https://doi.org/10.5194/acp-6-4321-2006, 2006.

Donahue, N. M., Robinson, A. L., Stanier, C. O., and Pandis, S. N.: Coupled Partitioning, Dilution, and Chemical Aging of Semivolatile Organics, Environmental Science & Technology, 40, 2635–2643, https://doi.org/10.1021/es052297c, 2006.

Elshorbany, Y., Barnes, I., Becker, K. H., Kleffmann, J., and Wiesen, P.: Sources and Cycling of Tropospheric Hydroxyl Radicals – An Overview, Zeitschrift für Physikalische Chemie, 224, 967–987, https://doi.org/10.1524/zpch.2010.6136, 2010.

Etminan, M., Myhre, G., Highwood, E. J., and Shine, K. P.: Radiative Forcing of Carbon Dioxide, Methane, and Nitrous Oxide: A Significant Revision of the Methane Radiative Forcing, Geophysical Research Letters, 43, 12,614–12,623, https://doi.org/10.1002/2016GL071930, 2016.

Eyring, V., Lamarque, J.-F., Hess, P., Arfeuille, F., Bowman, K., Chipperfiel, M. P., Duncan, B., Fiore, A., Gettelman, A., Giorgetta, M. A., Granier, C., Hegglin, M., Kinnison, D., Kunze, M., Langematz, U., Luo, B., Martin, R., Matthes, K., Newman, P. A., Peter, T., Robock, A., Ryerson, T., Saiz-Lopez, A., Salawitch, R., Schultz, M., Shepherd, T. G., Shindell, D., Staehelin, J., Tegtmeier, S., Thomason, L., Tilmes, S., Vernier, J.-P., Waugh, D., and Young, P. Y.: Overview of IGAC/SPARC Chemistry-Climate Model Initiative (CCMI) Community

520   Simulations in Support of Upcoming Ozone and Climate Assessments, SPARC Newsletter, 40, 48–66, 2013.

Field, C. B.: The Global Carbon Cycle: Integrating Humans, Climate, and the Natural World, no. v.62 in Scientific Committee on Problems of the Environment (SCOPE) Ser, Island Press, Washington, 2004.

Fiore, A. M., Dentener, F. J., Wild, O., Cuvelier, C., Schultz, M. G., Hess, P., Textor, C., Schulz, M., Doherty, R. M., Horowitz, L. W., MacKenzie, I. A., Sanderson, M. G., Shindell, D. T., Stevenson, D. S., Szopa, S., Van Dingenen, R., Zeng, G., Atherton, C., Bergmann,

525   D., Bey, I., Carmichael, G., Collins, W. J., Duncan, B. N., Faluvegi, G., Folberth, G., Gauss, M., Gong, S., Hauglustaine, D., Holloway, T., Isaksen, I. S. A., Jacob, D. J., Jonson, J. E., Kaminski, J. W., Keating, T. J., Lupu, A., Marmer, E., Montanaro, V., Park, R. J., Pitari, G., Pringle, K. J., Pyle, J. A., Schroeder, S., Vivanco, M. G., Wind, P., Wojcik, G., Wu, S., and Zuber, A.: Multimodel Estimates of Intercontinental Source-Receptor Relationships for Ozone Pollution, Journal of Geophysical Research: Atmospheres, 114, https://doi.org/10.1029/2008JD010816, 2009.

530   Fischer, E. V., Jacob, D. J., Millet, D. B., Yantosca, R. M., and Mao, J.: The Role of the Ocean in the Global Atmospheric Budget of Acetone, Geophysical Research Letters, 39, https://doi.org/10.1029/2011GL050086, 2012.

Forrest, M., Tost, H., Lelieveld, J., and Hickler, T.: Including Vegetation Dynamics in an Atmospheric Chemistry-Enabled General Circulation Model: Linking LPJ-GUESS (v4.0) with the EMAC Modelling System (v2.53), Geoscientific Model Development, 13, 1285–1309, https://doi.org/10.5194/gmd-13-1285-2020, 2020.

535   Forster, P., Ramaswamy, V., Artaxo, P., Berntsen, T., Betts, R., Fahey, D. W., Haywood, J., Lean, J., Lowe, D. C., Raga, G., Schulz, M., Dorland, R. V., Bodeker, G., Etheridge, D., Foukal, P., Fraser, P., Geller, M., Joos, F., Keeling, C. D., Keeling, R., Kinne, S., Lassey, K., Oram, D., O'Shaughnessy, K., Ramankutty, N., Reid, G., Rind, D., Rosenlof, K., Sausen, R., Schwarzkopf, D., Solanki, S. K., Stenchikov, G., Stuber, N., Takemura, T., Textor, C., Wang, R., Weiss, R., Whorf, T., Nakajima, T., Ramanathan, V., Ramaswamy, V., Artaxo, P., Berntsen, T., Betts, R., Fahey, D. W., Haywood, J., Lean, J., Lowe, D. C., Myhre, G., Nganga, J., Prinn, R., Raga, G., Schulz, M., and

540   Dorland, R. V.: Changes in Atmospheric Constituents and in Radiative Forcing.

Forster, P., Ramaswamy, V., Artaxo, P., Berntsen, T., Betts, R., Fahey, D. W., Haywood, J., Lean, J., Lowe, D. C., Myhre, G., Nganga, J., Prinn, R., Raga, G., Schulz, M., and Van Dorland, R.: Changes in Atmospheric Constituents and in Radiative Forcing, in: Climate Change 2007: The Physical Science Basis. Contribution of Working Group I to the Fourth Assessment Report of the Intergovernmental Panel on Climate Change, edited by Solomon, S., Qin, D., Manning, M., Chen, Z., Marquis, M., Averyt, K. B., Tignor, M., and Miller, H. L.,

545   Cambridge University Press, Cambridge, United Kingdom and New York, NY, USA, 2007.

Ganzeveld, L. and Lelieveld, J.: Impact of Amazonian Deforestation on Atmospheric Chemistry, Geophysical Research Letters, 31, https://doi.org/10.1029/2003GL019205, 2004.

Ganzeveld, L., Bouwman, L., Stehfest, E., van Vuuren, D. P., Eickhout, B., and Lelieveld, J.: Impact of Future Land Use and Land Cover Changes on Atmospheric Chemistry-Climate Interactions, Journal of Geophysical Research: Atmospheres, 115,

550   https://doi.org/10.1029/2010JD014041, 2010.

Gaudel, A., Cooper, O. R., Ancellet, G., Barret, B., Boynard, A., Burrows, J. P., Clerbaux, C., Coheur, P.-F., Cuesta, J., Cuevas, E., Doniki, S., Dufour, G., Ebojie, F., Foret, G., Garcia, O., Granados-Muñoz, M. J., Hannigan, J. W., Hase, F., Hassler, B., Huang, G., Hurtmans, D., Jaffe, D., Jones, N., Kalabokas, P., Kerridge, B., Kulawik, S., Latter, B., Leblanc, T., Le Flochmoën, E., Lin, W., Liu, J., Liu, X., Mahieu,

E., McClure-Begley, A., Neu, J. L., Osman, M., Palm, M., Petetin, H., Petropavlovskikh, I., Querel, R., Rahpoe, N., Rozanov, A., Schultz,
M. G., Schwab, J., Siddans, R., Smale, D., Steinbacher, M., Tanimoto, H., Tarasick, D. W., Thouret, V., Thompson, A. M., Trickl, T.,
Weatherhead, E., Wespes, C., Worden, H. M., Vigouroux, C., Xu, X., Zeng, G., and Ziemke, J.: Tropospheric Ozone Assessment Report:
Present-day Distribution and Trends of Tropospheric Ozone Relevant to Climate and Global Atmospheric Chemistry Model Evaluation,
Elementa: Science of the Anthropocene, 6, 39, https://doi.org/10.1525/elementa.291, 2018.

Gibbard, S., Caldeira, K., Bala, G., Phillips, T. J., and Wickett, M.: Climate Effects of Global Land Cover Change, Geophysical Research
Letters, 32, 2005GL024 550, https://doi.org/10.1029/2005GL024550, 2005.

Granier, C., Pétron, G., Müller, J.-F., and Brasseur, G.: The Impact of Natural and Anthropogenic Hydrocarbons on the Tropospheric Budget
of Carbon Monoxide, Atmospheric Environment, 34, 5255–5270, https://doi.org/10.1016/S1352-2310(00)00299-5, 2000.

Granier, C., Darras, S., Denier van Der Gon, H., Jana, D., Elguindi, N., Bo, G., Michael, G., Marc, G., Jalkanen, J.-P., Kuenen, J., Liousse,
C., Quack, B., Simpson, D., and Sindelarova, K.: The Copernicus Atmosphere Monitoring Service Global and Regional Emissions (April
2019 Version), Research Report, Copernicus Atmosphere Monitoring Service, https://doi.org/10.24380/d0bn-kx16, 2019.

Gromov, S., Jöckel, P., Sander, R., and Brenninkmeijer, C. a. M.: A Kinetic Chemistry Tagging Technique and Its Applica-
tion to Modelling the Stable Isotopic Composition of Atmospheric Trace Gases, Geoscientific Model Development, 3, 337–364,
https://doi.org/10.5194/gmd-3-337-2010, 2010.

Guelle, W., Schulz, M., Balkanski, Y., and Dentener, F.: Influence of the Source Formulation on Modeling the Atmospheric Global Distri-
bution of Sea Salt Aerosol, Journal of Geophysical Research: Atmospheres, 106, 27 509–27 524, https://doi.org/10.1029/2001JD900249,
2001.

Guenther, A., Hewitt, C. N., Erickson, D., Fall, R., Geron, C., Graedel, T., Harley, P., Klinger, L., Lerdau, M., Mckay, W. A., Pierce, T.,
Scholes, B., Steinbrecher, R., Tallamraju, R., Taylor, J., and Zimmerman, P.: A Global Model of Natural Volatile Organic Compound
Emissions, Journal of Geophysical Research: Atmospheres, 100, 8873–8892, https://doi.org/10.1029/94JD02950, 1995.

Guenther, A., Karl, T., Harley, P., Wiedinmyer, C., Palmer, P. I., and Geron, C.: Estimates of Global Terrestrial Isoprene Emissions
Using MEGAN (Model of Emissions of Gases and Aerosols from Nature), Atmospheric Chemistry and Physics, 6, 3181–3210,
https://doi.org/10.5194/acp-6-3181-2006, 2006.

Guenther, A. B., Zimmerman, P. R., Harley, P. C., Monson, R. K., and Fall, R.: Isoprene and Monoterpene Emission Rate
Variability: Model Evaluations and Sensitivity Analyses, Journal of Geophysical Research: Atmospheres, 98, 12 609–12 617,
https://doi.org/10.1029/93JD00527, 1993.

Hagemann, S.: An Improved Land Surface Parameter Dataset for Global and Regional Climate Models, https://doi.org/10.17617/2.2344576,
2002.

Heald, C. L. and Spracklen, D. V.: Land Use Change Impacts on Air Quality and Climate, Chemical Reviews, 115, 4476–4496,
https://doi.org/10.1021/cr500446g, 2015.

Heald, C. L., Henze, D. K., Horowitz, L. W., Feddema, J., Lamarque, J.-F., Guenther, A., Hess, P. G., Vitt, F., Seinfeld, J. H., Goldstein, A. H.,
and Fung, I.: Predicted Change in Global Secondary Organic Aerosol Concentrations in Response to Future Climate, Emissions, and Land
Use Change, Journal of Geophysical Research: Atmospheres, 113, 2007JD009 092, https://doi.org/10.1029/2007JD009092, 2008.

Hurtt, G. C., Chini, L. P., Frolking, S., Betts, R. A., Feddema, J., Fischer, G., Fisk, J. P., Hibbard, K., Houghton, R. A., Janetos, A., Jones,
C. D., Kindermann, G., Kinoshita, T., Klein Goldewijk, K., Riahi, K., Shevliakova, E., Smith, S., Stehfest, E., Thomson, A., Thornton, P.,
Van Vuuren, D. P., and Wang, Y. P.: Harmonization of Land-Use Scenarios for the Period 1500–2100: 600 Years of Global Gridded Annual

Land-Use Transitions, Wood Harvest, and Resulting Secondary Lands, Climatic Change, 109, 117–161, https://doi.org/10.1007/s10584-011-0153-2, 2011.

IUPAC: Evaluated kinetic data, https://iupac.aeris-data.fr/, accessed: 13 April 2025, 2025.

Jöckel, P., Sander, R., Kerkweg, A., Tost, H., and Lelieveld, J.: Technical Note: The Modular Earth Submodel System (MESSy) - a New
595   Approach towards Earth System Modeling, Atmospheric Chemistry and Physics, 5, 433–444, https://doi.org/10.5194/acp-5-433-2005, 2005.

Jöckel, P., Tost, H., Pozzer, A., Brühl, C., Buchholz, J., Ganzeveld, L., Hoor, P., Kerkweg, A., Lawrence, M. G., Sander, R., Steil, B., Stiller, G., Tanarhte, M., Taraborrelli, D., van Aardenne, J., and Lelieveld, J.: The Atmospheric Chemistry General Circulation Model ECHAM5/MESSy1: Consistent Simulation of Ozone from the Surface to the Mesosphere, Atmospheric Chemistry and Physics, 6, 5067–
600   5104, https://doi.org/10.5194/acp-6-5067-2006, 2006.

Keller, M., Jacob, D. J., Wofsy, S. C., and Harriss, R. C.: Effects of Tropical Deforestation on Global and Regional Atmospheric Chemistry, Climatic Change, 19, 139–158, https://doi.org/10.1007/BF00142221, 1991.

Kerkweg, A., Sander, R., Tost, H., and Jöckel, P.: Technical Note: Implementation of Prescribed (OFFLEM), Calculated (ONLEM), and Pseudo-Emissions (TNUDGE) of Chemical Species in the Modular Earth Submodel System (MESSy), Atmospheric Chemistry and
605   Physics, 6, 3603–3609, https://doi.org/10.5194/acp-6-3603-2006, 2006.

Klingmüller, K., Metzger, S., Abdelkader, M., Karydis, V. A., Stenchikov, G. L., Pozzer, A., and Lelieveld, J.: Revised Mineral Dust Emissions in the Atmospheric Chemistry–Climate Model EMAC (MESSy 2.52 DU_Astitha1 KKDU2017 Patch), Geoscientific Model Development, 11, 989–1008, https://doi.org/10.5194/gmd-11-989-2018, 2018.

Lana, A., Bell, T. G., Simó, R., Vallina, S. M., Ballabrera-Poy, J., Kettle, A. J., Dachs, J., Bopp, L., Saltzman, E. S., Stefels, J., Johnson, J. E.,
610   and Liss, P. S.: An Updated Climatology of Surface Dimethlysulfide Concentrations and Emission Fluxes in the Global Ocean, Global Biogeochemical Cycles, 25, https://doi.org/10.1029/2010GB003850, 2011.

Lelieveld, J., Butler, T. M., Crowley, J. N., Dillon, T. J., Fischer, H., Ganzeveld, L., Harder, H., Lawrence, M. G., Martinez, M., Taraborrelli, D., and Williams, J.: Atmospheric Oxidation Capacity Sustained by a Tropical Forest, Nature, 452, 737–740, https://doi.org/10.1038/nature06870, 2008.

615 Lelieveld, J., Gromov, S., Pozzer, A., and Taraborrelli, D.: Global Tropospheric Hydroxyl Distribution, Budget and Reactivity, Atmospheric Chemistry and Physics, 16, 12 477–12 493, https://doi.org/10.5194/acp-16-12477-2016, 2016.

Levy, H.: Normal Atmosphere: Large Radical and Formaldehyde Concentrations Predicted, Science, 173, 141–143, https://doi.org/10.1126/science.173.3992.141, 1971.

Li, M., Song, Y., Liu, M., Yao, H., Huang, X., Wang, X., and Zhang, Y.: Impacts of Decadal Variations in Natural Emissions
620   Due to Land-Cover Changes on Ozone Production in Southern China, Tellus B: Chemical and Physical Meteorology, 67, 27 676, https://doi.org/10.3402/tellusb.v67.27676, 2015.

Naik, V., Voulgarakis, A., Fiore, A. M., Horowitz, L. W., Lamarque, J.-F., Lin, M., Prather, M. J., Young, P. J., Bergmann, D., Cameron-Smith, P. J., Cionni, I., Collins, W. J., Dalsøren, S. B., Doherty, R., Eyring, V., Faluvegi, G., Folberth, G. A., Josse, B., Lee, Y. H., MacKenzie, I. A., Nagashima, T., van Noije, T. P. C., Plummer, D. A., Righi, M., Rumbold, S. T., Skeie, R., Shindell, D. T., Stevenson, D. S., Strode, S.,
625   Sudo, K., Szopa, S., and Zeng, G.: Preindustrial to Present-Day Changes in Tropospheric Hydroxyl Radical and Methane Lifetime from the Atmospheric Chemistry and Climate Model Intercomparison Project (ACCMIP), Atmospheric Chemistry and Physics, 13, 5277–5298, https://doi.org/10.5194/acp-13-5277-2013, 2013.

Nordeng, E. T.: Extended Versions of the Convective Parametrization Scheme at ECMWF and Their Impact on the Mean and Transient Activity of the Model in the Tropics., Research Department Technical Memorandum, 206, 1–41, 1994.

630   Nussbaumer, C. M., Crowley, J. N., Schuladen, J., Williams, J., Hafermann, S., Reiffs, A., Axinte, R., Harder, H., Ernest, C., Novelli, A., Sala, K., Martinez, M., Mallik, C., Tomsche, L., Plass-Dülmer, C., Bohn, B., Lelieveld, J., and Fischer, H.: Measurement Report: Photochemical Production and Loss Rates of Formaldehyde and Ozone across Europe, Atmospheric Chemistry and Physics, 21, 18 413–18 432, https://doi.org/10.5194/acp-21-18413-2021, 2021.

Nussbaumer, C. M., Fischer, H., Lelieveld, J., and Pozzer, A.: What controls ozone sensitivity in the upper tropical troposphere?, Atmospheric
635   Chemistry and Physics, 23, 12 651–12 669, https://doi.org/10.5194/acp-23-12651-2023, 2023.

Nussbaumer, C. M., Kohl, M., Pozzer, A., Tadic, I., Rohloff, R., Marno, D., Harder, H., Ziereis, H., Zahn, A., Obersteiner, F., Hofzumahaus, A., Fuchs, H., Künstler, C., Brune, W. H., Ryerson, T. B., Peischl, J., Thompson, C. R., Bourgeois, I., Lelieveld, J., and Fischer, H.: Ozone Formation Sensitivity to Precursors and Lightning in the Tropical Troposphere Based on Airborne Observations, Journal of Geophysical Research: Atmospheres, 129, e2024JD041 168, https://doi.org/10.1029/2024JD041168, 2024.

640   Pan, Y., Birdsey, R. A., Fang, J., Houghton, R., Kauppi, P. E., Kurz, W. A., Phillips, O. L., Shvidenko, A., Lewis, S. L., Canadell, J. G., Ciais, P., Jackson, R. B., Pacala, S. W., McGuire, A. D., Piao, S., Rautiainen, A., Sitch, S., and Hayes, D.: A Large and Persistent Carbon Sink in the World's Forests, Science, 333, 988–993, https://doi.org/10.1126/science.1201609, 2011.

Pöschl, U., von Kuhlmann, R., Poisson, N., and Crutzen, P. J.: Development and Intercomparison of Condensed Isoprene Oxidation Mechanisms for Global Atmospheric Modeling, Journal of Atmospheric Chemistry, 37, 29–52, https://doi.org/10.1023/A:1006391009798, 2000.

645   Pozzer, A., Jöckel, P., Sander, R., Ganzeveld, L., and Lelieveld, J.: Technical Note: The MESSy-submodel AIRSEA Calculating the Air-Sea Exchange of Chemical Species, 2006.

Pringle, K. J., Tost, H., Message, S., Steil, B., Giannadaki, D., Nenes, A., Fountoukis, C., Stier, P., Vignati, E., and Lelieveld, J.: Description and Evaluation of GMXe: A New Aerosol Submodel for Global Simulations (V1), Geoscientific Model Development, 3, 391–412, https://doi.org/10.5194/gmd-3-391-2010, 2010.

650   Randerson, J. T., Van Der Werf, G. R., Giglio, L., Collatz, G. J., and Kasibhatla, P. S.: Global Fire Emissions Database, Version 4.1 (GFEDv4), ORNL DAAC, https://doi.org/10.3334/ORNLDAAC/1293, 2015.

Roeckner, E., Brokopf, R., Esch, M., Giorgetta, M., Hagemann, S., Kornblueh, L., Manzini, E., Schlese, U., and Schulzweida, U.: Sensitivity of Simulated Climate to Horizontal and Vertical Resolution in the ECHAM5 Atmosphere Model, Journal of Climate, 19, 3771–3791, https://doi.org/10.1175/JCLI3824.1, 2006.

655   Sander, R., Baumgaertner, A., Cabrera-Perez, D., Frank, F., Gromov, S., Grooß, J.-U., Harder, H., Huijnen, V., Jöckel, P., Karydis, V. A., Niemeyer, K. E., Pozzer, A., Riede, H., Schultz, M. G., Taraborrelli, D., and Tauer, S.: The Community Atmospheric Chemistry Box Model CAABA/MECCA-4.0, Geoscientific Model Development, 12, 1365–1385, https://doi.org/10.5194/gmd-12-1365-2019, 2019.

Scott, C. E., Rap, A., Spracklen, D. V., Forster, P. M., Carslaw, K. S., Mann, G. W., Pringle, K. J., Kivekäs, N., Kulmala, M., Lihavainen, H., and Tunved, P.: The Direct and Indirect Radiative Effects of Biogenic Secondary Organic Aerosol, Atmospheric Chemistry and Physics,
660   14, 447–470, https://doi.org/10.5194/acp-14-447-2014, 2014.

Scott, C. E., Monks, S. A., Spracklen, D. V., Arnold, S. R., Forster, P. M., Rap, A., Äijälä, M., Artaxo, P., Carslaw, K. S., Chipperfield, M. P., Ehn, M., Gilardoni, S., Heikkinen, L., Kulmala, M., Petäjä, T., Reddington, C. L. S., Rizzo, L. V., Swietlicki, E., Vignati, E., and Wilson, C.: Impact on Short-Lived Climate Forcers Increases Projected Warming Due to Deforestation, Nature Communications, 9, 157, https://doi.org/10.1038/s41467-017-02412-4, 2018.

665   Smith, B., Prentice, I. C., and Sykes, M. T.: Representation of Vegetation Dynamics in the Modelling of Terrestrial Ecosystems: Comparing Two Contrasting Approaches within European Climate Space, Global Ecology and Biogeography, 10, 621–637, 2001.

Smith, B., Wårlind, D., Arneth, A., Hickler, T., Leadley, P., Siltberg, J., and Zaehle, S.: Implications of Incorporating N Cycling and N Limitations on Primary Production in an Individual-Based Dynamic Vegetation Model, Biogeosciences, 11, 2027–2054, https://doi.org/10.5194/bg-11-2027-2014, 2014.

670   Smith, C. J., Kramer, R. J., Myhre, G., Forster, P. M., Soden, B. J., Andrews, T., Boucher, O., Faluvegi, G., Fläschner, D., Hodnebrog, Ø., Kasoar, M., Kharin, V., Kirkevåg, A., Lamarque, J.-F., Mülmenstädt, J., Olivié, D., Richardson, T., Samset, B. H., Shindell, D., Stier, P., Takemura, T., Voulgarakis, A., and Watson-Parris, D.: Understanding Rapid Adjustments to Diverse Forcing Agents, Geophysical Research Letters, 45, 12,023–12,031, https://doi.org/10.1029/2018GL079826, 2018.

Spracklen, D. V., Jimenez, J. L., Carslaw, K. S., Worsnop, D. R., Evans, M. J., Mann, G. W., Zhang, Q., Canagaratna, M. R., Allan, J., Coe,
675   H., McFiggans, G., Rap, A., and Forster, P.: Aerosol Mass Spectrometer Constraint on the Global Secondary Organic Aerosol Budget, Atmospheric Chemistry and Physics, 11, 12 109–12 136, https://doi.org/10.5194/acp-11-12109-2011, 2011.

Stevenson, D. S., Young, P. J., Naik, V., Lamarque, J.-F., Shindell, D. T., Voulgarakis, A., Skeie, R. B., Dalsoren, S. B., Myhre, G., Berntsen, T. K., Folberth, G. A., Rumbold, S. T., Collins, W. J., MacKenzie, I. A., Doherty, R. M., Zeng, G., van Noije, T. P. C., Strunk, A., Bergmann, D., Cameron-Smith, P., Plummer, D. A., Strode, S. A., Horowitz, L., Lee, Y. H., Szopa, S., Sudo, K., Nagashima, T., Josse,
680   B., Cionni, I., Righi, M., Eyring, V., Conley, A., Bowman, K. W., Wild, O., and Archibald, A.: Tropospheric Ozone Changes, Radiative Forcing and Attribution to Emissions in the Atmospheric Chemistry and Climate Model Intercomparison Project (ACCMIP), Atmospheric Chemistry and Physics, 13, 3063–3085, https://doi.org/10.5194/acp-13-3063-2013, 2013.

Stevenson, D. S., Zhao, A., Naik, V., O'Connor, F. M., Tilmes, S., Zeng, G., Murray, L. T., Collins, W. J., Griffiths, P. T., Shim, S., Horowitz, L. W., Sentman, L. T., and Emmons, L.: Trends in Global Tropospheric Hydroxyl Radical and Methane Lifetime since 1850 from
685   AerChemMIP, Atmospheric Chemistry and Physics, 20, 12 905–12 920, https://doi.org/10.5194/acp-20-12905-2020, 2020.

Swann, A. L. S., Fung, I. Y., and Chiang, J. C. H.: Mid-Latitude Afforestation Shifts General Circulation and Tropical Precipitation, Proceedings of the National Academy of Sciences, 109, 712–716, https://doi.org/10.1073/pnas.1116706108, 2012.

Thornhill, G., Collins, W., Olivié, D., Skeie, R. B., Archibald, A., Bauer, S., Checa-Garcia, R., Fiedler, S., Folberth, G., Gjermundsen, A., Horowitz, L., Lamarque, J.-F., Michou, M., Mulcahy, J., Nabat, P., Naik, V., O'Connor, F. M., Paulot, F., Schulz, M., Scott, C. E., Séférian,
690   R., Smith, C., Takemura, T., Tilmes, S., Tsigaridis, K., and Weber, J.: Climate-Driven Chemistry and Aerosol Feedbacks in CMIP6 Earth System Models, Atmospheric Chemistry and Physics, 21, 1105–1126, https://doi.org/10.5194/acp-21-1105-2021, 2021.

Tiedtke, M.: A Comprehensive Mass Flux Scheme for Cumulus Parameterization in Large-Scale Models, 1989.

Tost, H., Jöckel, P., Kerkweg, A., Sander, R., and Lelieveld, J.: Technical Note: A New Comprehensive SCAVenging Submodel for Global Atmospheric Chemistry Modelling, Atmospheric Chemistry and Physics, 6, 565–574, https://doi.org/10.5194/acp-6-565-2006, 2006a.

695   Tost, H., Jöckel, P., and Lelieveld, J.: Influence of Different Convection Parameterisations in a GCM, Atmospheric Chemistry and Physics, 6, 5475–5493, https://doi.org/10.5194/acp-6-5475-2006, 2006b.

Tsimpidi, A. P., Karydis, V. A., Pozzer, A., Pandis, S. N., and Lelieveld, J.: ORACLE (v1.0): Module to Simulate the Organic Aerosol Composition and Evolution in the Atmosphere, Geoscientific Model Development, 7, 3153–3172, https://doi.org/10.5194/gmd-7-3153-2014, 2014.

700   Tsimpidi, A. P., Karydis, V. A., Pozzer, A., Pandis, S. N., and Lelieveld, J.: ORACLE 2-D (v2.0): An Efficient Module to Compute the Volatility and Oxygen Content of Organic Aerosol with a Global Chemistry–Climate Model, Geoscientific Model Development, 11, 3369–3389, https://doi.org/10.5194/gmd-11-3369-2018, 2018.

Unger, N.: Human Land-Use-Driven Reduction of Forest Volatiles Cools Global Climate, Nature Climate Change, 4, 907–910, https://doi.org/10.1038/nclimate2347, 2014.

705   Vella, R., Forrest, M., Lelieveld, J., and Tost, H.: Isoprene and Monoterpene Simulations Using the Chemistry–Climate Model EMAC (v2.55) with Interactive Vegetation from LPJ-GUESS (v4.0), Geoscientific Model Development, 16, 885–906, https://doi.org/10.5194/gmd-16-885-2023, 2023a.

Vella, R., Pozzer, A., Forrest, M., Lelieveld, J., Hickler, T., and Tost, H.: Changes in Biogenic Volatile Organic Compound Emissions in Response to the El Niño–Southern Oscillation, Biogeosciences, 20, 4391–4412, https://doi.org/10.5194/bg-20-4391-2023, 2023b.

710   Vella, R., Forrest, M., Pozzer, A., Tsimpidi, A. P., Hickler, T., Lelieveld, J., and Tost, H.: Influence of Land Cover Change on Atmospheric Organic Gases, Aerosols, and Radiative Effects, Atmospheric Chemistry and Physics, 25, 243–262, https://doi.org/10.5194/acp-25-243-2025, 2025.

Vicente-Serrano, S. M., Van Der Schrier, G., Beguería, S., Azorin-Molina, C., and Lopez-Moreno, J.-I.: Contribution of Precipitation and Reference Evapotranspiration to Drought Indices under Different Climates, Journal of Hydrology, 526, 42–54,
715   https://doi.org/10.1016/j.jhydrol.2014.11.025, 2015.

Voulgarakis, A., Naik, V., Lamarque, J.-F., Shindell, D. T., Young, P. J., Prather, M. J., Wild, O., Field, R. D., Bergmann, D., Cameron-Smith, P., Cionni, I., Collins, W. J., Dalsøren, S. B., Doherty, R. M., Eyring, V., Faluvegi, G., Folberth, G. A., Horowitz, L. W., Josse, B., MacKenzie, I. A., Nagashima, T., Plummer, D. A., Righi, M., Rumbold, S. T., Stevenson, D. S., Strode, S. A., Sudo, K., Szopa, S., and Zeng, G.: Analysis of Present Day and Future OH and Methane Lifetime in the ACCMIP Simulations, Atmospheric Chemistry and
720   Physics, 13, 2563–2587, https://doi.org/10.5194/acp-13-2563-2013, 2013.

Wang, L., Tai, A. P. K., Tam, C.-Y., Sadiq, M., Wang, P., and Cheung, K. K. W.: Impacts of Future Land Use and Land Cover Change on Mid-21st-Century Surface Ozone Air Quality: Distinguishing between the Biogeophysical and Biogeochemical Effects, Atmospheric Chemistry and Physics, 20, 11 349–11 369, https://doi.org/10.5194/acp-20-11349-2020, 2020.

Weber, J., King, J. A., Abraham, N. L., Grosvenor, D. P., Smith, C. J., Shin, Y. M., Lawrence, P., Roe, S., Beerling, D. J., and
725   Martin, M. V.: Chemistry-Albedo Feedbacks Offset up to a Third of Forestation's CO2 Removal Benefits, Science, 383, 860–864, https://doi.org/10.1126/science.adg6196, 2024.

Wu, S., Mickley, L. J., Kaplan, J. O., and Jacob, D. J.: Impacts of Changes in Land Use and Land Cover on Atmospheric Chemistry and Air Quality over the 21st Century, Atmospheric Chemistry and Physics, 12, 1597–1609, https://doi.org/10.5194/acp-12-1597-2012, 2012.